

University of Groningen

Dissecting the stellar content of Leo

Ruiz-Lara, T.; Gallart, C.; Monelli, M.; Fritz, T. K.; Battaglia, G.; Cassisi, S.; Aznar, M. Luis; Russo Cabrera, A. V.; Rodríguez-Martín, I.; Salazar-González, J. J.

Published in:
Monthly Notices of the Royal Astronomical Society

DOI:
[10.1093/mnras/staa3871](https://doi.org/10.1093/mnras/staa3871)

IMPORTANT NOTE: You are advised to consult the publisher's version (publisher's PDF) if you wish to cite from it. Please check the document version below.

Document Version
Publisher's PDF, also known as Version of record

Publication date:
2021

[Link to publication in University of Groningen/UMCG research database](#)

Citation for published version (APA):

Ruiz-Lara, T., Gallart, C., Monelli, M., Fritz, T. K., Battaglia, G., Cassisi, S., Aznar, M. L., Russo Cabrera, A. V., Rodríguez-Martín, I., & Salazar-González, J. J. (2021). Dissecting the stellar content of Leo: A dwarf irregular caught in transition. *Monthly Notices of the Royal Astronomical Society*, 501(3), 3962-3980. <https://doi.org/10.1093/mnras/staa3871>

Copyright

Other than for strictly personal use, it is not permitted to download or to forward/distribute the text or part of it without the consent of the author(s) and/or copyright holder(s), unless the work is under an open content license (like Creative Commons).

The publication may also be distributed here under the terms of Article 25fa of the Dutch Copyright Act, indicated by the "Taverne" license. More information can be found on the University of Groningen website: <https://www.rug.nl/library/open-access/self-archiving-pure/taverne-amendment>.

Take-down policy

If you believe that this document breaches copyright please contact us providing details, and we will remove access to the work immediately and investigate your claim.

Downloaded from the University of Groningen/UMCG research database (Pure): <http://www.rug.nl/research/portal>. For technical reasons the number of authors shown on this cover page is limited to 10 maximum.

Dissecting the stellar content of Leo I: a dwarf irregular caught in transition

T. Ruiz-Lara¹,^{1,2,3}★ C. Gallart,^{2,3} M. Monelli¹,^{2,3} T. K. Fritz,^{2,3} G. Battaglia,^{2,3} S. Cassisi,^{4,5} M. Luis Aznar,² A. V. Russo Cabrera¹,^{2,6} I. Rodríguez-Martín⁷ and J. J. Salazar-González⁷

¹Kapteyn Astronomical Institute, University of Groningen, Landleven 12, NL-9747 AD Groningen, the Netherlands

²Instituto de Astrofísica de Canarias, Calle Vía Láctea s/n, E-38205 La Laguna, Tenerife, Spain

³Departamento de Astrofísica, Universidad de La Laguna, E-38200 La Laguna, Tenerife, Spain

⁴INAF – Astronomical Observatory of Abruzzo, via M. Maggini, sn, I-64100 Teramo, Italy

⁵INFN, Sezione di Pisa, Largo Pontecorvo 3, I-56127 Pisa, Italy

⁶Grupo de Operaciones de Ingeniería, Gran Telescopio de Canarias, Cuesta de San José, s/n, E-38712 Breña Baja, La Palma, Spain

⁷Dpto. de Matemáticas, Estadística e Investigación Operativa, Universidad de La Laguna, E-38200 La Laguna, Tenerife, Spain

Accepted 2020 November 24. Received 2020 November 24; in original form 2020 October 13

ABSTRACT

Leo I is considered one of the youngest dwarf spheroidals (dSph) in the Local Group. Its isolation, extended star formation history (SFH), and recent perigalacticon passage (~ 1 Gyr ago) make Leo I one of the most interesting nearby stellar systems. Here, we analyse deep photometric *Hubble Space Telescope* data via colour–magnitude diagram fitting techniques to study its global and radially resolved SFH. We find global star formation enhancements in Leo I ~ 13 , 5.5, 2.0, and 1.0 Gyr ago, after which it was substantially quenched. Within the context of previous works focused on Leo I, we interpret the most ancient and the youngest ones as being linked to an early formation (surviving reionization) and the latest perigalacticon passage (transition from dIrr to dSph), respectively. We clearly identify the presence of very metal poor stars ($[\text{Fe}/\text{H}] \sim -2$) ageing ~ 5 – 6 and ~ 13 Gyr old. We speculate with the possibility that this metal-poor population in Leo I is related to the merging with a low-mass system (possibly an ultra-faint dwarf). This event would have triggered star formation (peak of star formation ~ 5.5 Gyr ago) and accumulated old, metal-poor stars from the accreted system in Leo I. Some of the stars born during this event would also form from accreted gas of low-metallicity (giving rise to the 5–6 Gyr low-metallicity tail). Given the intensity and extension of the 2.0 Gyr burst, we hypothesize that this enhancement could also have an external origin. Despite the quenching of star formation around 1 Gyr ago (most probably induced by ram pressure stripping with the Milky Way halo at pericentre), we report the existence of stars as young as 300–500 Myr. We also distinguish two clear spatial regions: the inner ~ 190 pc presents a homogeneous stellar content (size of the gaseous star forming disc in Leo I from ~ 4.5 to 1 Gyr ago), whereas the outer regions display a clear positive age gradient.

Key words: methods: observational – techniques: spectroscopic – galaxies: evolution – galaxies: formation – galaxies: kinematics and dynamics – galaxies: stellar content.

1 INTRODUCTION

The interest on galaxies in the low-mass end of the galaxy population has been vigorous in the last decades (e.g. Mateo 1998; Gallart et al. 1999a; Battaglia et al. 2006; Belokurov et al. 2007; Tolstoy, Hill & Tosi 2009; Monelli et al. 2010a; Boylan-Kolchin, Bullock & Kaplinghat 2011; Hidalgo et al. 2011; Weisz et al. 2011; McConnachie 2012; Kirby et al. 2013). This raising interest is well founded. On one hand, dwarf galaxies, the most common kind in the Universe, have masses in rough agreement with the critical mass of the first galaxies that turned into the building blocks of the stellar haloes of present-day massive galaxies (e.g. Peebles 1965;

see Dayal & Ferrara 2018 for a review). Indeed, some of the dwarf galaxies that we currently observe in the Local Group could be analogues of the first dwarf galaxies to exist in the Universe and are survivors of such an early epoch. On the other hand, the study of dwarf galaxies is crucial to improve cosmological models of galaxy formation on small scales, where baryon physics involved in star formation, inflows and outflows, or stellar feedback need to be properly described (e.g. Silk & Mamon 2012; Di Cintio et al. 2014; Dutton et al. 2016). As such, the characterization of the stars populating these systems as well as of their star formation histories¹ (SFHs), is of the utmost importance to understand, not only dwarf

¹In this work, we will consider the star formation history of a stellar system as the evolution with the cosmic time of both the SFR and the chemical enrichment (AMR).

* E-mail: tomasruizlara@gmail.com

galaxy evolution (Tolstoy et al. 2009; Gallart et al. 2015), but the evolution of the Universe as a whole from its earliest epochs (e.g. Weisz et al. 2014b; Benítez-Llambay et al. 2015; Monelli et al. 2016).

Dwarf galaxies have been classified historically in dwarf spheroidal galaxies (dSph), transition types (dT) or irregular (dIrr), mainly based on their *current* morphology as observed in optical bands (from smooth and spheroidal to patchy and irregular); and gas and young stellar content (absence to richness). It seems natural that, based on this classification, dwarf galaxies evolve with time from dIrr to dT and finally to dSph. In this process, the environment where they evolve should play an important role as well (as indicated by the morphology–density relation found in the Local Group; Grebel 1999). However, a classification based on their complete SFH (actual evolution) should provide a more complete and precise view on how these systems form and evolve. In this line, Gallart et al. (2015), using data from the LCID project,² proposed a new classification of dwarf galaxies as ‘*slow*’ or ‘*fast*’. *Fast* dwarfs would be composed mainly by old stars, outcome of a short and intense early star formation, whereas *slow* dwarfs would only form a small fraction of their stellar mass at early epochs, presenting an extended SFH running up to (nearly) the present time. Taking into account the location and inferred orbits of the studied dwarfs, Gallart et al. (2015) proposed that the ultimate origin of the dichotomic SFHs, and thus of the two dwarf galaxy types, would be related to the density of the environment where each dwarf formed, being the ‘*slow*’ or ‘*fast*’ nature imprinted at formation. Later evolution (inflows, outflows, dwarf–dwarf interactions, interaction with host galaxy, feedback, etc.) would further delineate the evolution and current properties of ‘*slow*’ dwarfs. This includes a possible environmentally induced late star formation quenching that could give a ‘*slow*’ dwarf, with an evolutionary history much alike that of a classical dIrr galaxy, the current appearance of a classical dSph. As a consequence, the analysis of the stellar content of *slow* dwarfs, identified as those with substantial star formation beyond 10 Gyr or so, is of special importance.

Having formed stars since the very beginning up to advanced stages in the evolution of the Universe, the study of dwarf galaxies with extended SFHs can help us in understanding the complex interplay between halo growth, reionization, star formation, stellar feedback, and environmental effects. When and how these galaxy evolution drivers affect dwarf galaxies depend on the specifics of each system at different stages of its evolution, and imprint different signatures in their SFHs. In particular, it is known that this evolution can induce internal spatial variations of the stellar content characteristics in dwarf galaxies.

Dwarf galaxies tend to be younger and more metal rich in their inner parts than in their outskirts, where stars are older and more metal poor (e.g. Battaglia et al. 2006; Faria et al. 2007; Beccari et al. 2014; del Pino, Aparicio & Hidalgo 2015; Okamoto et al. 2017). These stellar populations gradients have been shown to exist since very early epochs, from the radial variation of the properties of the old RR Lyrae variable stars in ‘*fast*’ galaxies (e.g. Bernard et al. 2008; Martínez-Vázquez et al. 2015). Their existence can be explained as a consequence of the shrinking of the star forming disc in dwarf galaxies, radial migration, and ejection of stars via supernova feedback (Stinson et al. 2009; Graus et al. 2019). Indeed, Graus et al. (2019) found, making use of cosmological simulations, that dwarf

galaxies with large dark matter cores display flatter age profiles as a consequence of the effect of late-time feedback (extended SFH), predicting clear relations between radial changes in the SFH of dwarf galaxies and their dark matter halo distribution. Unfortunately, precise analysis of the spatial variation of extended SFH in dwarf galaxies exist only for a handful of systems (e.g. Hidalgo et al. 2013).

Leo I is one of the most distant Milky Way satellites, and it is classified as a dSph galaxy (McConnachie 2012) based on its current morphology and lack of gas (Knapp, Kerr & Bowers 1978; Grcevich & Putman 2009), or as a ‘*slow*’ galaxy based on its full SFH (Gallart et al. 2015). Indeed, Leo I displays a very extended SFH (Gallart et al. 1999a; Hernandez, Gilmore & Valls-Gabaud 2000), and is considered one of the youngest dSph in our Local Group in terms of average age (see Lee et al. 1993) together with Leo A (Cole et al. 2007; Ruiz-Lara et al. 2018) or the Aquarius dwarf irregular galaxy (DDO210; Cole et al. 2014). Indeed, its oldest population remained elusive for some time (Held et al. 2000) and most of Leo I star-forming activity happened between 7 and as recently as 1 Gyr ago (Gallart et al. 1999a). At such point, Leo I stopped forming stars probably linked to the pericentric approach to the Milky Way ~ 1 Gyr ago, as indicated by the careful analysis of the proper motion of Leo I stars and derived orbit (Sohn et al. 2013). The dating of this pericentric passage of Leo I has been recently confirmed using Gaia DR2 (Gaia Collaboration 2018a) data (Fritz et al. 2018; Gaia Collaboration 2018b). Thus, it seems that Leo I has just been caught in transition between dIrr to dSph. But this is just its most recent history. Previous works have hinted a turbulent past characterized by alternated periods of intense star formation with quiescent intervals (Gallart et al. 1999a; Hernandez et al. 2000). All this, combined with the narrow stellar metallicity displayed by Leo I, its shallow negative metallicity gradient and positive age trend (Gullieuszik et al. 2009), make of Leo I one of the most exciting dwarf galaxies in the Local Group. However, most of the efforts at characterizing the SFH of Leo I made use of old observations from the Wide Field Planetary Camera II (WFPC2) on board of the *Hubble Space Telescope* (*HST*), dating more than 2 decades back (Gallart et al. 1999a; Hernandez et al. 2000; Dolphin 2002; Weisz et al. 2014b, 2015). A whole new characterization of its SFH, with updated and deeper data and powerful analysis techniques will allow us to fully unveil the sequence of events shaping Leo I, improving the age resolution of previous works and determining precise chemical enrichment histories. A summary of the main properties of this system can be found in Table 1.

With this goal in mind, in this work we use novel colour–magnitude diagram (CMD) fitting techniques to analyse a modern and extremely deep *HST* Advanced Camera for Surveys (ACS) data set, reaching well below the oldest main-sequence turn-off with an unprecedented precise photometry. The combination of updated techniques and stellar evolutionary models, together with this exquisite data set, will indeed improve the age resolution from previous works and to characterize the chemical enrichment of Leo I as never before. Here, we revise the global SFH of Leo I, adding important new insights as well as determine the radially resolved SFH of Leo I. This paper is structured as follows: Section 2 describes the data as well as the data reduction. A qualitative analysis of the observed CMD of Leo I is provided in Section 3 whereas a quantitative study of its SFH (globally and radially) is given in Sections 4 and 5. The results are discussed in Section 6 and the conclusions outlined in Section 7.

²<http://research.iac.es/proyecto/LCID/>

Table 1. Leo I main properties.

Parameter (1)	Value (2)	Reference (3)
RA (J2000)	10 ^h 08 ^m 28 ^s .1	i
Dec. (J2000)	+12° 18′ 23″	i
<i>l</i>	226.0	i
<i>b</i>	+49.1	i
Distance (kpc)	254	ii
(<i>m</i> − <i>M</i>) ₀	22.02	ii
<i>M</i> _V	−12.0 ± 0.3	iii
<i>M</i> _* (M _⊙)	5.5 × 10 ⁶	i
<i>M</i> _* / <i>L</i> _V	4.4	iv
<i>M</i> _{H I} (M _⊙)	<0.03 × 10 ⁶	v
<i>M</i> _{dyn} (<i>R</i> _{vir}) (M _⊙)	(7 ± 1) × 10 ⁸	vi
<i>V</i> _{sys} (km s ^{−1})	282.9 ± 0.5	vi
<i>E</i> (<i>B</i> − <i>V</i>)	0.036	i
<i>R</i> _{vir} (kpc)	18.3 ± 2.7	vi
<i>R</i> _{tidal} (pc)	935 ± 140	iii
<i>R</i> _{1/2light} (pc)	251 ± 27	iii
Ellipticity	0.21	iii
Position angle (°)	79	iii
[Fe/H]	−1.43 ± 0.01	vii

Note. References: i – McConnachie (2012); ii – Bellazzini et al. (2004); iii – Irwin & Hatzidimitriou (1995); iv – Muñoz et al. (2018); v – Grevesch & Putman (2009); vi – Mateo, Olszewski & Walker (2008); vii – Kirby et al. (2011).

2 DATA SETS AND REDUCTION PROCESS

Images of Leo I were retrieved from the *HST* archive, and were originally collected by two projects: GO10520³ and GO12270.⁴ In both cases, the ACS was pointing the innermost region, though slightly off-centred, while the parallel WFC3 were located to the north (see Fig. 1). In the case of the ACS (WFC3), a total integration time of 10 200 (8091) s and 27 297 (8491) s, was devoted to the *F435W* (*F438W*) and *F814W* filters, respectively. Detailed logs are presented in Table 2.

2.1 Data reduction

The photometric reduction was performed using the DAOPHOTIV and ALLFRAME suite of programmes (Stetson 1987, 1994), using the same approach for both the ACS and WFC3 data (see Monelli et al. 2010a, for a detailed description of the procedure). Individual empirical point spread functions (PSFs) were derived for individual chip of each image, with semi-automatic iterative routines. The input list of stars for ALLFRAME was generated on a median, cosmic rays cleaned stacked image. ALLFRAME fits the empirical PSFs to candidate sources on individual images, producing a catalogue of positions and instrumental magnitudes for each image. The final list of sources was obtained cross-matching individual files, retaining objects detected in at least (*half* + 1) of the images. The final photometric lists contain 191 756 and 8956 sources for the ACS and the WFC3 fields. Instrumental magnitudes were calibrated to the VEGAMAG system using appropriate zero-points available on each instrument web page.

Artificial stars tests (ASTs) were performed following (following Monelli et al. 2010a). The 2 × 10⁶ stars injected in each chip, in

many runs with few thousand stars each were drawn from a synthetic CMD covering well the observed one, and similar to the one that will be used to derive the SFH. Artificial stars were distributed in a regular grid and spaced avoiding overlap of the PSF’s wings. The photometry was repeated identically as for the original data. ASTs provide fundamental information to simulate the photometric errors in the synthetic CMD used to derive the SFH (see Section 4).

As already commented, previous determinations of the SFH of Leo I (Gallart et al. 1999a; Hernandez et al. 2000; Dolphin 2002; Weisz et al. 2014b, 2015), all made use of old data collected using the WFPC2@*HST*. For a complete account of such observations, we encourage the reader to check Gallart et al. (1999b). A quick comparison between both data sets is outlined here. WFPC2 observations used filters *F555W* and *F814W*, whereas the ACS data set analysed here uses filters *F435W* and *F814W*. The broader colour baseline of the data analysed in this work plays an important role at separating different stellar populations using CMD fitting. In addition, ACS observations clearly have larger exposure times as compared to the WFPC2 data (10 200 and 27 297 seconds compared to 6300 and 5100 seconds, blue, and red filters, respectively). This ends up with our CMDs being populated by 191 756 stars compared to the 28 000 stars with reliable photometry from WFPC2 (as can be seen from Fig. 1, the old WFPC2 field is almost fully embedded within the new ACS field). Finally, while WFPC2 data hardly reaches oMSTO (near *I*-band 26 mag according to Gallart et al. 1999b), the CMD presented in Fig. 2 reaches well below the oMSTO, and down to *F814W* ~5 mag with reliable photometry (40 per cent completeness according to our ASTs). We have shown in Ruiz-Lara et al. (2018) that the analysis of CMDs of a similar depth to the ones observed with WFPC2 present clear disadvantages with respect to deeper CMDs when recovering SFHs, especially at old ages.

The improvements of the here-analysed photometric data set and our analysis will allow us to achieve an unprecedented age resolution and AMR reconstruction. The coupling of all these factors will result on a unique opportunity to pinpoint key events and fully unveil the past history of Leo I.

3 THE LEO I COLOUR–MAGNITUDE DIAGRAM

Fig. 2 shows the derived ACS (*F814W*, *F435W* − *F814W*) CMD, which spans over 9 mag, from the tip of the red giant branch (RGB, *F814W* ~ −3 mag) down to about 2 mag fainter than the oldest main-sequence (MS) turn-off (oMSTO), and it reveals many features strongly suggesting a complex SFH. The well-populated faintest sub-giant branch (SGB) and RGB suggest an important fraction of old population, supported by the clear detection of a blue horizontal branch (HB). Nevertheless, the MS extends as a conspicuous sequence to bluer colour and brighter magnitude, indicating, together with the well-populated red clump (RC), the presence of an important intermediate-age population. Interestingly, brighter than the old SGB, at least two other SGB are clearly visible, separated by regions with lower density of points, suggesting a gasping SFH, with alternating periods of enhanced and more quiet star formation. Finally, the blue MS stars, reaching above the HB level, together with the presence of blue-loop stars, suggest the presence of a small population younger than 1 Gyr.

To further constrain the properties of the stellar populations in Leo I, Fig. 2 presents the superposition of model predictions from the BaSTI data base⁵ (Pietrinferni et al. 2004, the same used for the

³Resolving the Complex Star Formation History of the Leo I Dwarf Spheroidal Galaxy, P.I. T. Smecker-Hane.

⁴Proper Motion of Leo I: Constraining the Milky Way Mass, P.I. S. Sohn.

⁵<http://basti.iaa.es/teramo.inaf.it/index.html>

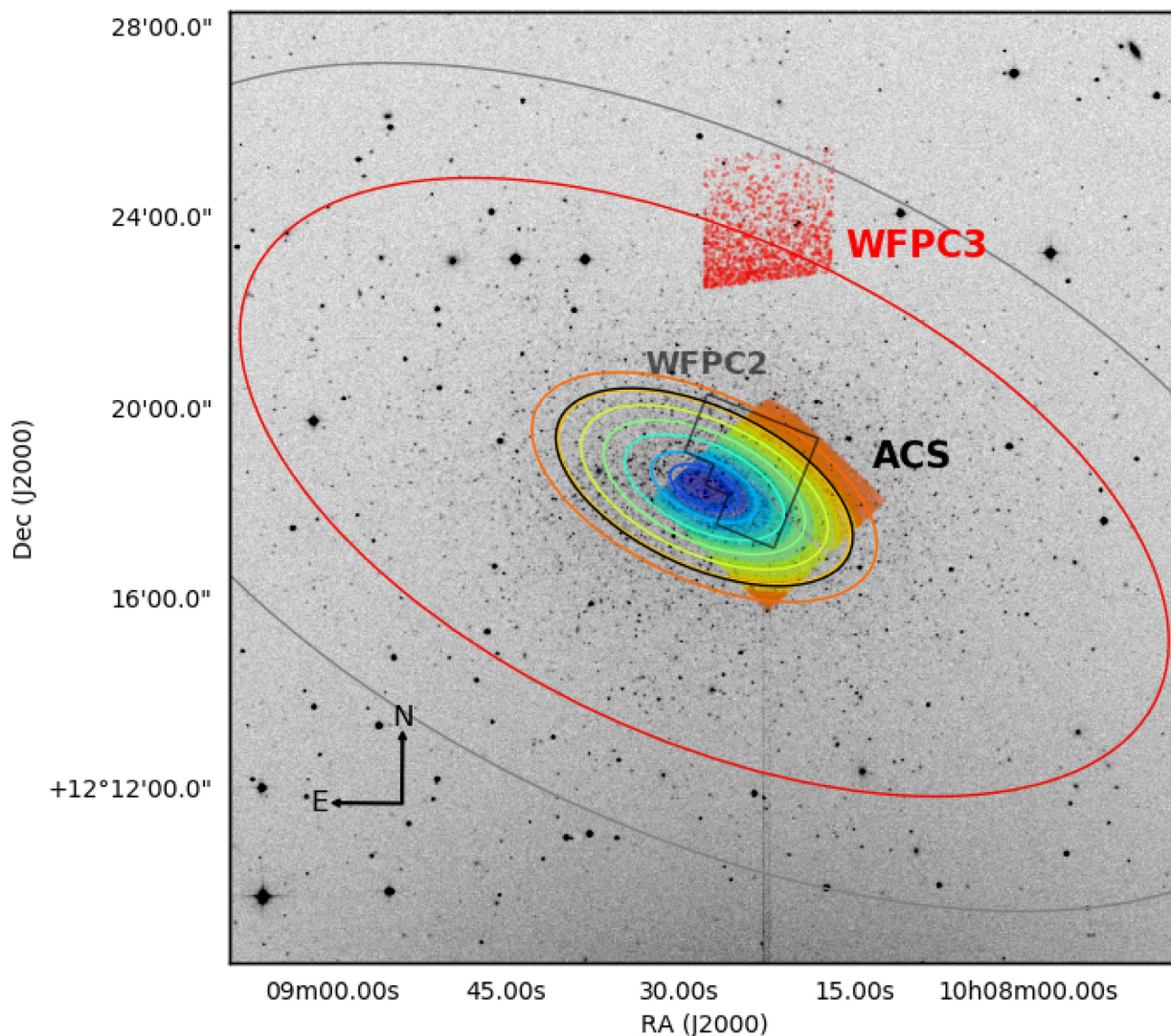


Figure 1. Leo I observational layout. Spatial distribution of stars analysed in this work, colour-coded according to its radial distance (see Table 3), superimposed to a DSS r -band image of the Leo I dwarf galaxy. The main ACS field, together with the parallel WFC3 field, can be easily outlined (see Section 2). The black and grey ellipses depict the half-light and tidal radius, respectively. For completeness, we have added the footprint (grey polygon) of the WFC2@HST data analysed in previous determinations of the SFH of Leo I (i.e. Gallart et al. 1999a; Hernandez et al. 2000; Dolphin 2002; Weisz et al. 2014a, b).

quantitative derivation of SFH, see Section 4). The left-hand panel shows the superposition of the zero-age horizontal branch (ZAHB) for two metallicities, $Z = 0.0006, 0.002$. The two sequences bracket the luminosity the HB stars over the whole colour range, suggesting a metallicity spread. The right-hand panel presents the superposition of isochrones for the labelled ages and metallicities. The comparison suggests the presence of an old (~ 10 – 13 Gyr) and relatively metal-poor ($Z = 0.0003$, $[\text{Fe}/\text{H}] \sim -1.8$) population. The second SGB is well represented by a 5 Gyr, slightly more metal-rich isochrone, while the upper SGB is compatible with a 2 Gyr, $Z = 0.001$ ($[\text{Fe}/\text{H}] \sim -1.2$) population. Few tenths of magnitude below the luminosity level of the HB, the MS seems to present a quite sharp drop in stellar counts, suggesting a decrease in the star formation rate (SFR) around 1 Gyr ago (green isochrone). Nevertheless, the magenta isochrone represents well the upper MS and the blue loop with a population of ~ 300 Myr, although the dark green one shows that we cannot exclude the presence of some stars as young as 100 Myr.

Such a comparison, while enlightening about the Leo I stellar content, suffers from two main problems: (i) it is qualitative, in the

sense that it can identify the presence of stellar populations, but it does not provide a quantitative estimate of the amount of mass formed; (ii) it suffers from degeneracy between age and metallicity, such that isochrones with different combinations of these parameters can represent certain features in the CMD equally well. To overcome these problems, a detailed quantitative SFH is derived in Section 4.

4 THE GLOBAL LEO I STAR FORMATION HISTORY

The quantitative analysis of the SFH of extended regions within dwarf galaxies is crucial to understand the past history of these systems, dating and characterizing their main evolutionary events. In this section, we derive the SFH of the central region of Leo I (ACS field, see Fig. 1), while the possible spatial differences will be discussed in Section 5. The larger number of stars used for the global analysis enables the proper assessment of the reliability and robustness of the SFH recovery method that is presented in Appendix A.

Table 2. Log of the observations. (1) Image name; (2) name of the filter; (3) exposure time; (4) time (UT) of the start of the exposure; (5) identifier of the observing programme.

Name	Filter	Exp. time (s)	UT start	Prog. ID
(1)	(2)	(3)	(4)	(5)
ACS data				
j9gz01orq	F435W	1700.0	2006-02-10 09:38:31	10520
j9gz01oxq	F435W	1700.0	2006-02-10 14:22:51	10520
j9gz02tiq	F435W	1700.0	2006-02-18 06:18:54	10520
j9gz02tjq	F435W	1700.0	2006-02-18 07:50:23	10520
j9gz02tlq	F435W	1700.0	2006-02-18 09:26:19	10520
j9gz02tnq	F435W	1700.0	2006-02-18 11:02:15	10520
j9gz03tqq	F435W	1700.0	2006-02-18 12:39:33	10520
j9gz04tsq	F814W	1700.0	2006-02-18 14:17:56	10520
j9gz04ttq	F814W	1700.0	2006-02-18 15:50:04	10520
j9gz04tvq	F814W	1700.0	2006-02-18 17:26:01	10520
j9gz05tyq	F814W	1700.0	2006-02-18 19:06:10	10520
j9gz05tzq	F814W	1700.0	2006-02-18 20:41:09	10520
j9gz05u1q	F814W	1700.0	2006-02-18 22:18:22	10520
j9gz06krq	F814W	440.0	2006-01-26 06:35:01	10520
j9gz06ksq	F814W	440.0	2006-01-26 06:45:01	10520
j9gz06kuq	F814W	440.0	2006-01-26 08:07:31	10520
bjjm01kkq	F814W	1267.0	2011-01-25 11:46:18	12270
bjjm01kmq	F814W	1267.0	2011-01-25 12:10:03	12270
bjjm01kpq	F814W	1361.0	2011-01-25 13:18:10	12270
bjjm01ktq	F814W	1360.0	2011-01-25 13:43:29	12270
bjjm02kyq	F814W	1267.0	2011-01-25 14:58:04	12270
bjjm02l0q	F814W	1267.0	2011-01-25 15:21:49	12270
bjjm02l3q	F814W	1363.0	2011-01-25 16:29:57	12270
bjjm02l7q	F814W	1364.0	2011-01-25 16:55:18	12270
bjjm03lcq	F814W	1267.0	2011-01-25 18:09:50	12270
bjjm03leq	F814W	1267.0	2011-01-25 18:33:35	12270
bjjm03lhq	F814W	1363.0	2011-01-25 19:41:43	12270
bjjm03llq	F814W	1364.0	2011-01-25 20:07:04	12270
WFC3 data				
ibjm01klq	F814W	1326.0	2011-01-25 11:45:23	12270
ibjm01knq	F438W	1367.0	2011-01-25 12:10:24	12270
ibjm01kqq	F814W	1371.0	2011-01-25 13:18:25	12270
ibjm01kuq	F438W	1466.0	2011-01-25 13:43:50	12270
ibjm02kzq	F814W	1326.0	2011-01-25 14:57:09	12270
ibjm02l1q	F438W	1367.0	2011-01-25 15:22:10	12270
ibjm02l4q	F814W	1371.0	2011-01-25 16:30:12	12270
ibjm02l8q	F438W	1462.0	2011-01-25 16:55:39	12270
ibjm03ldq	F814W	1326.0	2011-01-25 18:08:55	12270
ibjm03lfq	F438W	1367.0	2011-01-25 18:33:56	12270
ibjm03liq	F814W	1371.0	2011-01-25 19:41:58	12270
ibjm03lmq	F438W	1462.0	2011-01-25 20:07:25	12270

In this work, we recover SFHs by comparing observed and synthetic CMDs⁶ following the methodology carefully outlined in Monelli et al. (2010a). In short, we define simple stellar populations (SSPs, using an age-metallicity grid) from synthetic CMDs to then obtain the combination of these SSPs that better reproduce observed diagrams. However, prior to the comparison itself there are a series of steps that need to be followed. First, we simulate observational effects (incompleteness and photometric errors) on the synthetic CMD based on the ASTs presented in Section 2.1. For this, we use a specifically designed code named `DisPar` (see Appendix B). We then seek the linear combination of SSPs that best fits the observed CMD.

⁶Directly derived from stellar evolution models with the assumption of stellar population parameters and bolometric corrections.

This is done using the code `THESTORM` (‘Tracing tHe Evolution of the STar fOrmation Rate and Metallicity’), thoroughly described in Bernard et al. (2015, 2018). `THESTORM` compares the number of stars in colour–magnitude boxes of different sizes depending on their location within the observed and synthetic CMDs (a ‘bundle’ strategy defines the colour–magnitude grid, with the size of the boxes in each bundle determining its importance in the fit, see Fig. 3). In addition, `THESTORM` carries out this comparison several times by applying shifts (i) to the observed CMDs with respect to the synthetic CMD in colour and magnitude to assess possible uncertainties in the photometry, photometric zero-points, distance, or reddening vector, anchoring the observed CMD to the position where the minimum χ^2 is found ($[\Delta(\text{colour})_{\min}, \Delta(\text{Mag})_{\min}]$); (ii) in the colour–magnitude grid sampling the stars in the CMD; and (iii) in the age–metallicity grid defining the SSP. The multiple SFHs calculated applying these shifts are combined in the final solution, and used in the calculation of the uncertainties in the SFR and age–metallicity relation (AMR), following Hidalgo et al. (2011).

Here, we use synthetic CMDs⁷ computed using the BaSTI, solar scaled stellar evolution library (Pietrinferni et al. 2004, using bolometric corrections for the ACS and WFC3 passbands). They are composed by 50 million stars with ages between 0.03 and 14.0 Gyr and metallicities ranging from 0.0001 to 0.008 (covering the whole range of expected values for Leo I). We also assumed a Kroupa initial mass fraction (Kroupa 2001), an unresolved binary fraction of 50 per cent (β), a minimum mass ratio for binaries of 0.1 (q), and a Reimers mass-loss parameter of 0.2 (η) for the computation of this synthetic CMD. Then, we divide the synthetic CMD according to the following basic age–metallicity grid to define the different SSPs:

Age: [0.03; 0.05; 0.1–1.0 in steps of 0.1; 1.2–2.0 in steps of 0.2; 2.5–6.0 in steps of 0.5; 7.0–14.0 in steps of 1] Gyr

Metallicity: [1, 2, 4, 7, 1.1, 1.6, 2.2, 2.9, 3.7, 4.6, 5.6, 6.7, 8.0] $\times 10^{-4}$

The bundle strategy is depicted in Fig. 3 (left-hand panel), superimposed in the observed CMD of Leo I, together best model (middle panel) and the residuals (right-hand panel). The bundles are designed to include in the fit most of the observed stars (i.e. most of the observed stars are within the ‘bundles’) with at least 1 mag deeper than the location of the oMSTO (something that the photometric depth and accuracy of the analysed data allow). Small boxes (larger weight) are used in the bundles covering the better-modelled and denser MS region (bundle #3), whereas larger boxes (less weight) are used in the bright MS (bundle #2), RGB and RC regions (bundles #4 and #5, respectively) as well as a region bluer than the blue end of the MS (bundle #1). The sizes of the boxes in each bundle are given in the table on the central panel of Fig. 3, where the best-fitting CMD is represented. Finally, the right-hand panel shows the residuals CMD. Note the quality of the fit, particularly in the MS region. Some differences in the area of the CMD dominated by helium-burning stars appear. These are due to two main effects: (i) on the one hand, the BaSTI models adopted in this work use conductive opacity prescriptions that can be improved, slightly decreasing the brightness of HB stellar models (Cassisi et al. 2007; Hidalgo et al. 2018); (ii) on the other hand, implementation of a variable mass-loss efficiency during the RGB stage is preferable while computing synthetic CMDs (Savino et al. 2019) rather than a fixed one as in

⁷Synthetic CMDs are computed using an adapted version of the synthetic CMD code available at the BaSTI webpage (<http://basti.iaa-teramo.inaf.it/in dex.html>). This code allows the user to obtain synthetic CMDs for a given photometric system and with flat distributions in age and metallicity.

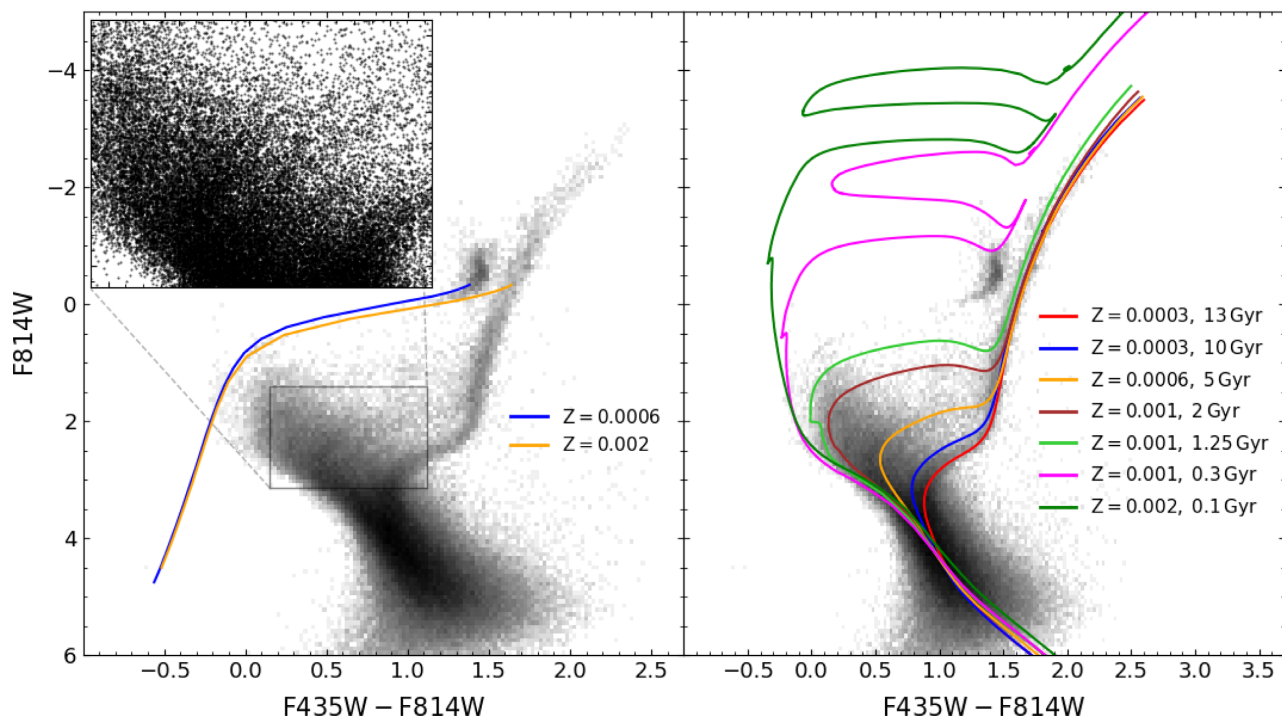


Figure 2. Observed M_{F814W} and $M_{F435W}-M_{F814W}$ colour–magnitude diagram from the ACS field in Leo I. Left-hand panel: Observed CMD with the ZAHB loci for metallicities of 0.002 and 0.0006 ($[\text{Fe}/\text{H}] \sim -0.96$ and -1.49 , respectively), overlaid. To highlight the level of details that can be observed in the diagram, in particular the different and well-differentiated sub-giant branches departing from the main sequence, this panel includes an inset zooming in the region of the MSTOs. Right-hand panel: This time we overlay a set of theoretical isochrones to the observed diagram. Ages and metallicities of these isochrones range from 100 Myr to 13 Gyr and from $Z = 0.002$ ($[\text{Fe}/\text{H}] \sim -0.96$) to $Z = 0.0003$ ($[\text{Fe}/\text{H}] \sim -1.78$), respectively. Adopted distance modulus and reddening as provided in Table 1.

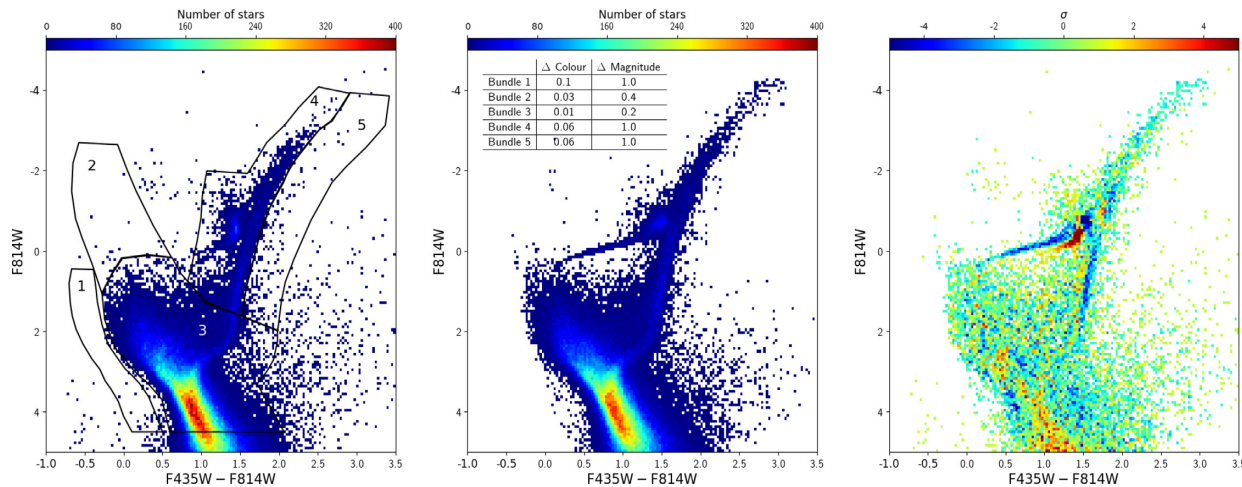


Figure 3. Colour–magnitude diagram fitting example and ‘bundle’ strategy. From left to right: observed CMD (ACS field) with the bundles overlotted; (ii) best-fitting CMD with a table showing the dimensions of the boxes in each bundle for the star counting; and (iii) residual CMD (observed – best fit) in Poissonian sigmas.

this case ($\eta = 0.2$, Reimers mass-loss parameter). This has a small effect mainly in the colour distribution of stars along the core He-burning sequence. The low weight given during the fit to these conflict areas minimizes its effect on the SFH recovery. During the course of this project, we have also carefully tested the effect of the β and q parameters defining the binary star population in the synthetic CMD, and that of the bundle strategy on the SFH recovery. Appendix A summarizes all these tests, legitimates the above-described choice and expands on the adopted bundle strategy. The chosen approach is that named ‘A2’ in Appendix A. The position of the $[\Delta(\text{colour})]_{\min}$,

$\Delta(\text{Mag})_{\min}$ was found at [0.03, 0.00] in the fitting of the ACS CMD.

Fig. 4 shows the SFH derived for the region within Leo I observed with the ACS, corresponding to the parametrization of the CMDs described above (red). For completeness, we also show all the solutions for all the tests (black, see Appendix A). Note the robustness of the technique as all the solutions are compatible within errors. The main characteristics displayed by the Leo I SFH are in common to all the tests, indicating that these results are independent on the details of the method. We find that Leo I has experienced an extended SFH

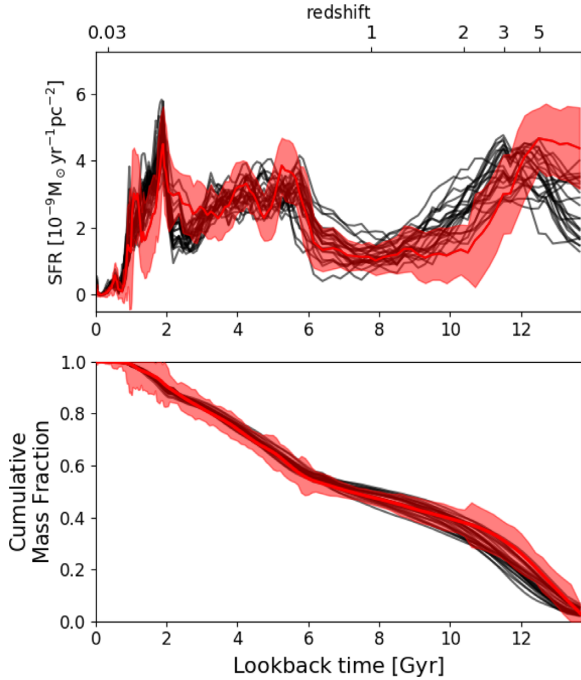


Figure 4. Global SFH recovered from the ACS field (central parts) of Leo I. Top: SFR as a function of time. Bottom: cumulative mass fraction. In red we highlight the best solution (A2). Nevertheless, we show the solutions from all different tests (see Appendix A) in black.

characterized by conspicuous star formation enhancements (0.4–0.65, 1.0–1.28, 1.65–2.5, 3.7–5.9, 10.5–13.7 Gyr ago). After the first prolonged star-forming episode (older than ~ 10 Gyr), an epoch of low star formation follows until ~ 6 Gyr ago when star formation is heavily reignited. A more abrupt quenching of the star formation activity can be clearly observed around 1 Gyr ago, when the SFR is compatible with zero except for a well-defined burst 0.5 Gyr ago. The causes and interpretation of this peculiar behaviour will be discussed in Section 6.

The bottom panel of Fig. 4 shows the cumulative SFH, indicative of a nearly constant average SFH, except for the initial and final periods. Note that even though this kind of representation is useful for a broad characterization of the evolution of the stellar mass content in a galaxy, it does not capture many rich and robust details of its SFH that can be associated with important events in its evolution, as will be discussed in Section 6.

The recovered AMR is one of the main novelties of this work and is shown in Fig. 5 as an age–metallicity density map. We observe chemical enrichment from $[\text{Fe}/\text{H}]$ values close to ~ -1.9 for the oldest stars in Leo I to ~ -0.75 for the youngest. We can distinguish two clear epochs of rapid chemical enrichment from ~ 13 to 10 Gyr ago and from 2.5 to 1 Gyr. After that, the average stellar metallicity seems to slightly decrease (although this is an uncertain feature given the low number of stars younger than 1 Gyr found in the solution). For stars with intermediate-to-old ages (~ 2.5 –10 Gyr) little or no chemical enrichment is found. Specially striking is the spread in metallicity shown by stars of ages older than 11 Gyr and between 5 and 6 Gyr, both coinciding with two important star forming periods. Another clear deviation from the general trend can be found at age ~ 9 Gyr and $[\text{Fe}/\text{H}] \sim -0.9$. However, whereas the first feature (metal-poor tail at ages ~ 5 –6 and >11 Gyr) can be observed in all tests shown in Fig. 4 and is considered reliable, this second one disappears in most of the cases and thus, it is not real but a natural

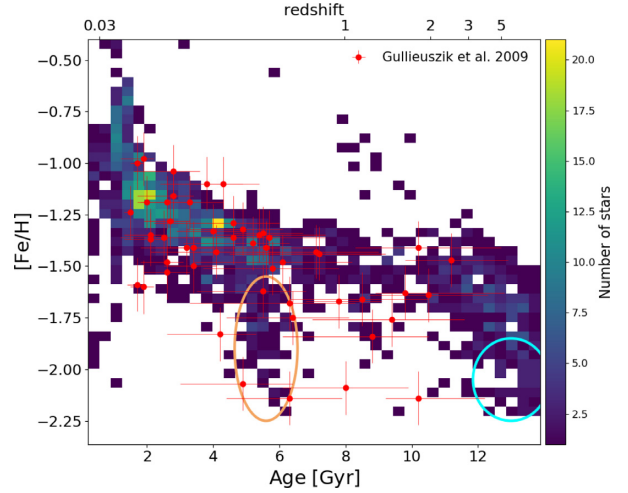


Figure 5. Global AMR recovered from the ACS field (central parts) of Leo I (best solution, A2). On top of the solution presented in this work (coloured density map), we show the measurements from 54 RGB stars presented in Gullieuszik et al. 2009 (red points with errorbars). Ellipses highlight the tail of old, metal-poor stars (cyan) and that found around 5–6 Gyr ago (brown), interpreted as signs of a merger between Leo I and an ultra-faint-like dwarf galaxy (see Section 6 for details).

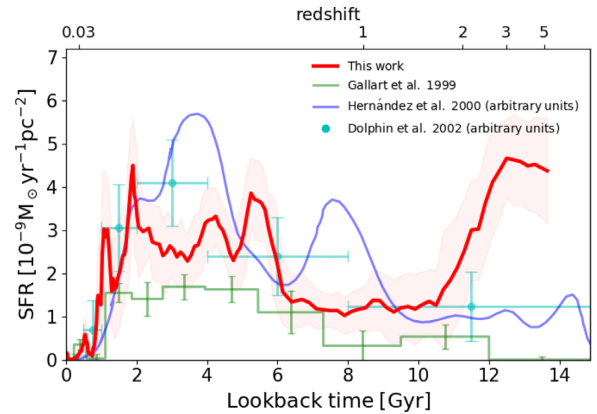


Figure 6. Comparison between SFH determinations from previous works. We compare the best solution (A2), with those presented in Gallart et al. (1999a, green), Hernandez et al. (2000, blue), and Dolphin (2002), all using old data from WFPC2@HST. In the case of the Hernandez et al. (2000) and Dolphin (2002) determination the SFR has been normalized to arbitrary units.

fluctuation within the fitting procedure. Fig. 5 also compares the recovered AMR with the information on ages and metallicities of 54 RGB stars from the analysis of spectroscopic data in the Ca II triplet region (Gullieuszik et al. 2009). The resemblance between both approaches is remarkable, especially mimicking the low-metallicity tail at ~ 5 –6 Gyr. The large age uncertainties affecting giant stars, together with the scarcity of stars (low SFR), makes the region between 7 and 10 Gyr more uncertain, but still compatible between both approaches.

This SFH is in broad agreement with the main features found in previous determinations (e.g. Gallart et al. 1999a; Hernandez et al. 2000; Dolphin 2002), and particularly with the presence of an important amount of intermediate-age population, the increase of the SFR occurred $\simeq 6$ Gyr ago, and the quenching $\simeq 1$ Gyr ago (see Fig. 6). Gallart et al. (1999a) even recover the small star formation burst occurred $\simeq 0.5$ Gyr ago. These previous studies, however, tend

Table 3. Radial analysis of the Leo I SFH. (1) Identifier of the radial region; (2) and (3) radial extension in arcmins and parsecs; (4) number of stars within each region; (5) area of the region (in pc²); (6) instrument; (7) average (standard deviation) stellar age from the synthetic stars in the best-fitting model; (8) average (standard deviation) stellar [Fe/H] from the best-fitting model.

Region	Extension		Number of stars	Area	Instrument	Average (σ) age	Average (σ) [Fe/H]
(1)	(arcmin)	(pc)	(4)	(pc ²)	(6)	(Gyr)	(dex)
(1)	(2)	(3)	(4)	(5)	(6)	(7)	(8)
1	0.0–0.67	0.0–49.4	17 339	3702	ACS	6.8 (4.3)	−1.54 (0.32)
2	0.5–1.08	36.9–79.7	27 668	6241	ACS	6.8 (4.4)	−1.51 (0.34)
3	1.0–1.58	73.8–116.6	32 934	8144	ACS	6.9 (4.3)	−1.51 (0.33)
4	1.5–2.08	110.7–153.5	33 411	9596	ACS	6.8 (4.3)	−1.47 (0.34)
5	2.0–2.58	147.6–190.4	33 111	10 628	ACS	6.8 (4.2)	−1.47 (0.34)
6	2.5–3.08	184.5–227.3	31 862	11 546	ACS	7.0 (4.3)	−1.47 (0.36)
7	3.0–3.67	221.4–270.8	25 828	10 107	ACS	7.3 (4.3)	−1.49 (0.38)
8	3.5–4.58	258.3–338.0	24 775	10 945	ACS	7.6 (4.4)	−1.46 (0.40)
9	~10.5	~771.8	3969	38 920	WFC3	10.4 (3.4)	−1.67 (0.41)

to find a substantially lower level of star formation at old ages, compared to what they find at intermediate ages, at odds with the present study. One might think that this could be partially due to the fact that the early determinations of the Leo I SFH were based on *HST* WFPC2 data that covered a central, smaller field of view than the current ACS data. However, as will be shown in Section 5 below, we also find a high old SFR in the innermost parts of the analysed field. We conclude that it is the shallow CMD provided by the WFPC2 data that prevent previous works to fully unveil the old stellar populations (see Section 2 for a comparison between both datasets). Interestingly, Hernandez et al. (2000) find a peak of star formation at ~ 8 Gyr, where we find a sustained, low level of star formation (see Section 6 for a discussion on this). Dolphin (2002) claimed that the largest and more intense period of star formation expands from 3 to 1 Gyr ago, in agreement with two of our detected peaks. Overall, our SFH offers a much more detailed view of the evolution of Leo I with an unprecedented age resolution, including the metallicity evolution and the oldest population in Leo I, which are poorly investigated in these previous studies due to the limited depth of the WFPC2 data set.

5 A RADIAL VIEW ON THE LEO I EVOLUTION

Given the limited spatial coverage of our data, the SFH presented in Section 4 might not be representative of the Leo I dwarf galaxy as a whole, especially in the presence of stellar population gradients in Leo I. A wealth of observational evidence exists suggesting that the presence of such radial gradients are ubiquitous (e.g. Held et al. 2000; Harbeck et al. 2001; Tolstoy et al. 2004; Battaglia et al. 2006, 2012a, b; Beccari et al. 2014; McMonigal et al. 2014; del Pino et al. 2015; Santana et al. 2016; Okamoto et al. 2017). In this sense, simulations are finally finding the presence of age gradients in simulated galaxies, with older stars dominating the outer parts Graus et al. (e.g. 2019). As such, the SFH presented in Fig. 4 might be biased to young ages if similar gradients exist in Leo I (e.g. Gullieuszik et al. 2009; Held et al. 2010), not providing a global view characteristic of this dwarf galaxy. The authors also suggest that the region around the half-light radius can be used as a good proxy for such global SFH. Fortunately, the analysed ACS data cover this region (~ 250 pc from its centre; McConnachie 2012) and its quality allows us to study it separately (purpose of this section). In addition, a spatially resolved study of the Leo I SFH can provide further insight on its build-up and evolution.

With this aim in mind, and benefiting from the exquisite quality of the analysed data (ACS and WFC3 parallel field; see Section 2),

we split the ACS observed field into eight spatial regions. We adopted an elliptical isophotal binning scheme to define the different spatial regions under analysis. The elliptical apertures were centred at $10^{\text{h}}08^{\text{m}}28^{\text{s}}.1$, $+12^{\circ}18'23''$ (J2000; McConnachie 2012) with PA = 79° , $\epsilon = 0.21$ (Irwin & Hatzidimitriou 1995) and partially overlap (Hidalgo et al. 2013). We preferred to use overlapping regions to increase the spatial sampling having a good number of stars in each aperture and to smooth out statistical fluctuations. The widths of the different apertures were varied accordingly as a compromise between the number of stars in each bin ($\sim 20\,000$ – $30\,000$) and the radial sampling of the ACS field. Finally, the most external region (region 9) is given by the location of the WFC3 parallel field and was analysed as a whole due to its low number of stars. These regions are overlaid to a DSS *r*-band image in Fig. 1 and relevant information is given in Table 3. All the observed CMDs for each spatial region can be found in Fig. 7.

We apply the same methodology explained before to obtain the SFH from the nine observed radial CMDs. We follow the same bundle + synthetic CMD strategy (see Section 4 and Appendix A) and we have anchored the solution to the $[\Delta(\text{colour})_{\text{min}}, \Delta(\text{Mag})_{\text{min}}]$ found for the analysis of the whole Leo I ACS CMD ($[0.03, 0.00]$). This restriction allows us to properly compare the average age and, especially, metallicity between different radial regions, such that the differences found are only attributable to real changes in their stellar content. Nine different ‘dispersed’ synthetic CMDs (one for each region) are generated from the above-described synthetic CMD after simulating errors. The ASTs used in this section have also been divided radially in the same eight apertures under analysis (ACS field) in order to be representative of the conditions in each radial bin. In the case of the parallel WFC3 field, it has been analysed as a whole (3969 stars after quality cuts in χ^2 and *sharp* parameter are applied), using their own ASTs and a synthetic CMD computed for the WFC3 passbands.

Fig. 8 shows the recovered SFH for the nine spatial regions. A common pattern can be clearly observed in all regions in agreement to the global SFH features described in Section 4. An initial epoch of intense star formation (continuing to 10 Gyr ago) is followed by a period of lower star forming activity, after which star formation is reignited, with prominent burst ~ 5.5 , 4, 2, 1, and 0.5 Gyr ago. However, some differences can be found when comparing the inner with the outer regions. Whereas in the inner ~ 190 pc (regions 1–5, upper panel) such bursts coexist with an important background star formation, in the outer regions star formation is mainly concentrated in these star bursting events. This is also reflected in the cumulative representation of the SFH shown in the lower panel of Fig. 8, where

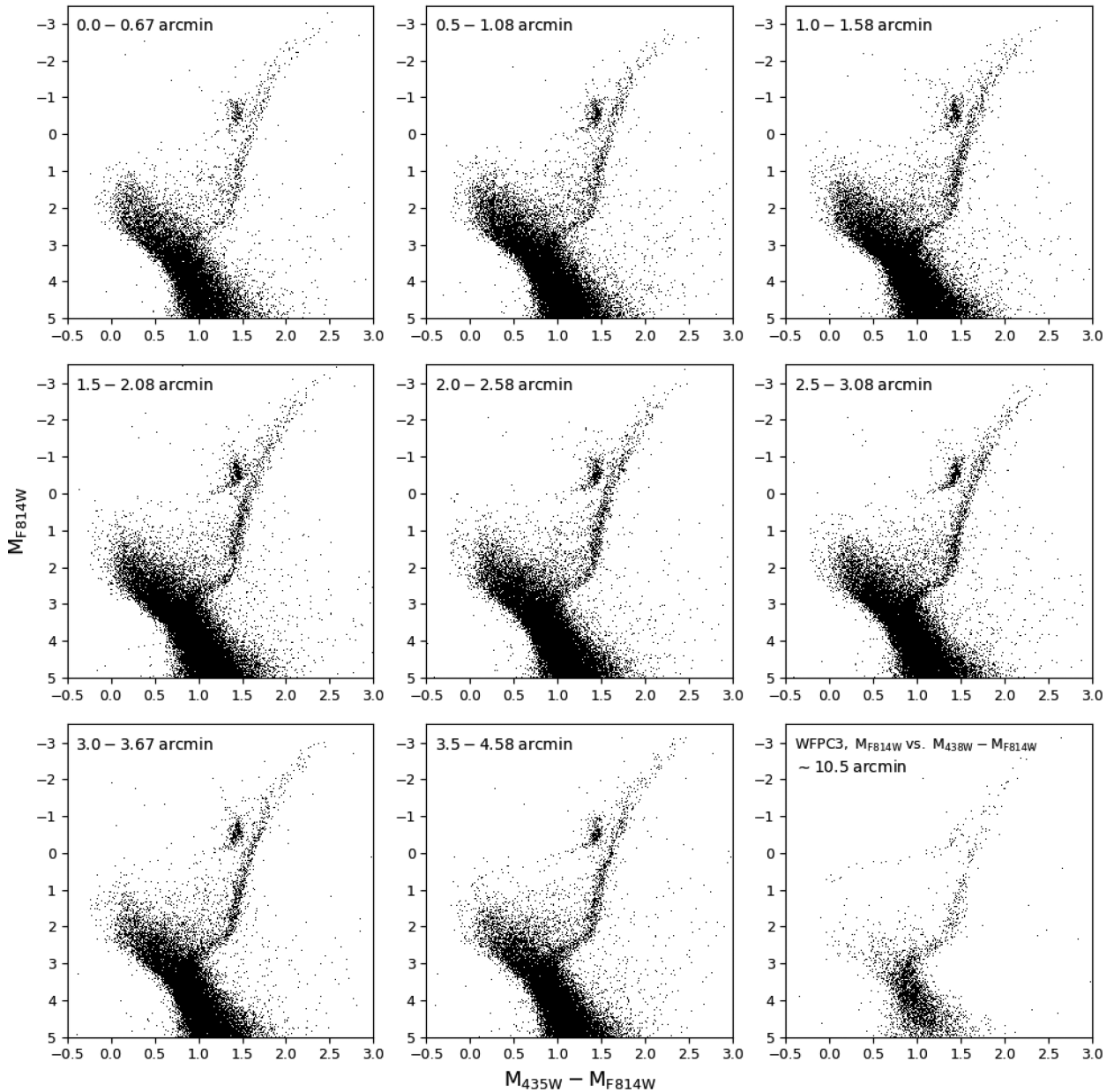


Figure 7. Observed colour–magnitude diagrams used in the analysis of the spatial variation of the Leo I SFH. Galactocentric distance increases from the top-left to the bottom-right, being this last one the outermost, WFC3 parallel field. Colour–magnitude combinations are M_{F814W} and $M_{F435W} - M_{F814W}$ for the ACS fields and M_{F814W} and $M_{F438W} - M_{F814W}$ for the WFC3 field.

the lines corresponding to regions 6–9 depart from the almost straight line characteristic of the central Leo I SFH. It is particularly striking that the periods of enhanced star formation are found in all regions, *including the outermost region 9*, that is dominated by old stars ($\simeq 90$ percent and 80 percent of star formation occurred prior to 6 Gyr ago and 10 Gyr ago, respectively).

This dichotomy between inner and outer parts is clearly highlighted in Fig. 9 as well, which expands on the radial distribution of the stars associated with the above-defined star formation epochs. It also displays the Leo I stellar mean age profile. Both the fraction of stars in each population within particular age ranges indicated in the left-hand panel of Fig. 9 (coloured, dashed lines) and the age profile (black, solid line), display a flat trend up to ~ 190 pc from the centre where they depart from it. Older average ages are found

in these outermost regions mainly due to a decrease in the presence of stars younger than ~ 4 –6 Gyr and the lack of star formation in between bursts (i.e. 2–4 Gyr). These findings support the idea of an outside-in shrinking of the gaseous star forming disc (Stinson et al. 2009) avoiding star formation in the outer parts in the last ~ 4 –6 Gyr, except maybe at the time of the previously described bursts (probably linked to violent events, see Section 6). However, the possibility exists that (as found in Graus et al. 2019) outer stars with ages compatible with the reported bursts (~ 5.5 , 4, 2, 1, and 0.5 Gyr) migrated to outer radii due to stellar feedback. Table 3 also shows the average stellar ages and [Fe/H] values (together with the standard deviations) of the stars populations regions 1–9 according to their corresponding best models. We see also here the above-mentioned dichotomy in the stellar age. The [Fe/H] values display

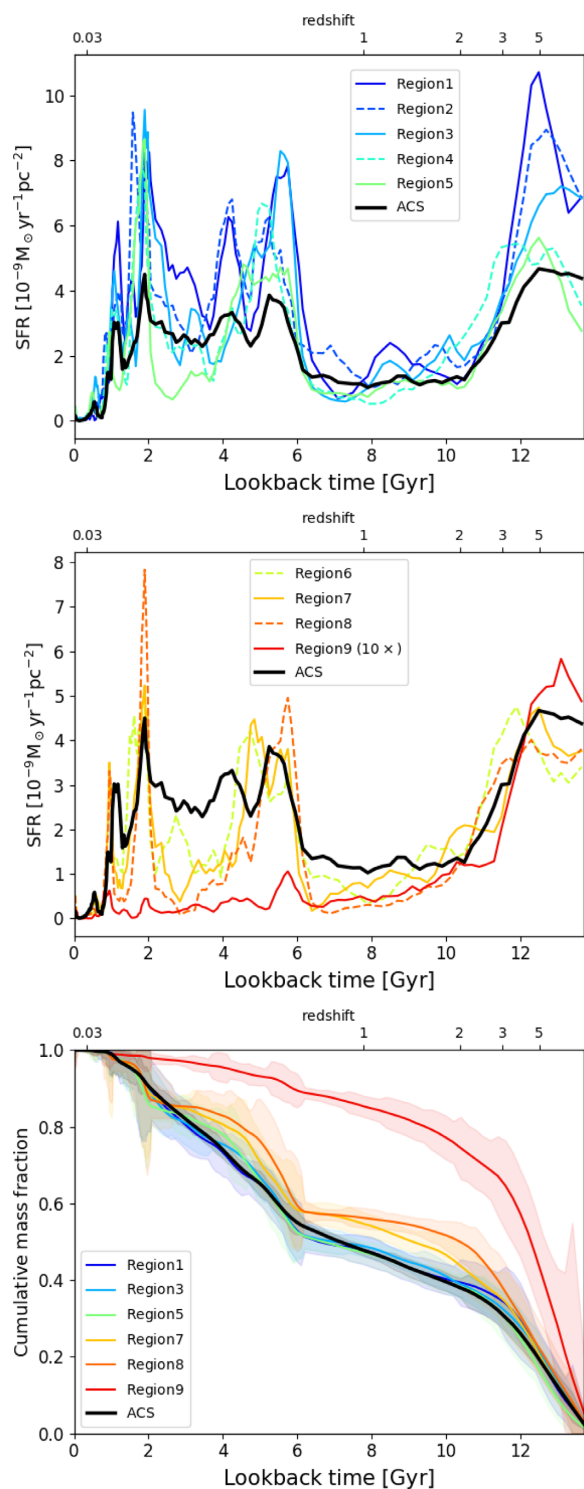


Figure 8. Radial variation of the SFH in Leo I. Left and middle panels show the SFR as a function of lookback time for the innermost and outermost regions, respectively. Right-hand panel displays the cumulative mass fractions for a set of radial apertures. As a reference, we have added to all plots the solution from the whole ACS field (A2 test, in black). Given the low SFR values found in region 9 we have applied a 10× factor for visualization purposes.

an almost null gradient (considering the large dispersion of values), consistent with Gullieuszik et al. (2009).

6 DISCUSSION

The thorough characterization of the stellar populations of Leo I carried out in this work has further unveiled the complexity of this system, enabling an unprecedented understanding of its past. In this section, we will discuss the possible physical origin of the different features of the Leo I SFH, from the oldest to the most recent ones, both in terms of the star formation and metallicity evolution. A graphical representation of the evolutionary scenario drawn from the results of this study is shown in Fig. 11.

Reionization has long been thought to play an important role in the early evolutionary stages of dwarf galaxies (e.g. Efstathiou 1992; Gnedin 2000). In particular, it is expected to be able to regulate, and even truncate, star formation in low mass systems (Hoeft et al. 2006; Okamoto, Gao & Theuns 2008). Models predict that the UV background produced during reionization (occurring at redshift ~ 7 ; Planck Collaboration XLVII 2016) is capable of heating the gas and even driving it out of low-mass haloes, quenching star formation (Benítez-Llambay et al. 2015). However, there is evidence indicating that reionization alone cannot completely stop star formation in *classical* dwarf galaxies with stellar masses comparable with that of Leo I (above $10^6 M_{\odot}$; Monelli et al. 2010a, b; Hidalgo et al. 2011). On the contrary, the simultaneous combination of internal stellar feedback and reionization could completely halt star formation in dwarf galaxies (Benítez-Llambay et al. 2015). We show here that Leo I is a survivor of reionization. The recovered SFH is compatible with a first peak of star formation occurring ~ 12 Gyr ago, with lower (or constant) values of SFR previous to that main peak (see Fig. 4), possibly indicating self-regulation at early times. Whether the survival of Leo I after reionization was due to its already relatively high mass or to its formation in a relatively isolated environment with infrequent mergers is beyond the reach of this analysis.

After this initial phase in which Leo I survived reionization and the possible later peak in star formation (~ 12 Gyr ago), it entered a quiescent epoch (10–6 Gyr ago) characterized by the presence of a lower than average level of star formation. It is well known that observational errors and the intrinsic limitations of the adopted methodology can affect our ability to recover well-defined bursts of star formation at old ages (Rusakov et al. 2020). In addition, Hernandez et al. (2000) recover a conspicuous peak of star formation at ~ 8 Gyr in this epoch where we find this quiescent period. Ruiz-Lara et al. (2020) studied the ability of CMD-fitting techniques to recover star forming bursts in terms of time, duration, and age resolution. As a consequence, we have decided to further investigate the presence of the low-level star formation in the 10–6 Gyr age range through a series of tests using mock stellar populations (see Fig. 10). For that purpose, we have created synthetic CMDs mimicking both observational errors and the recovered SFH for the Leo I ACS field (see Fig. 4), adding some modifications in the ~ 7 –11 Gyr age range. In one test, we have removed all the stars in that range (see blue line in Fig. 10). In the others, we added stars in the 8.5–9.5 Gyr range to mimic the presence of a burst of different strengths (green, lime, and orange lines). After applying our SFH recovery methodology to the CMDs of these mock stellar populations, we can conclude that we cannot reproduce the observed behaviour neither with a total absence of stars in the 7–11 Gyr range nor with the presence of a star forming burst within that range. These tests confirm that Leo I kept a low, but sustained, level of star formation from ~ 10 Gyr ago up to 6 Gyr ago.

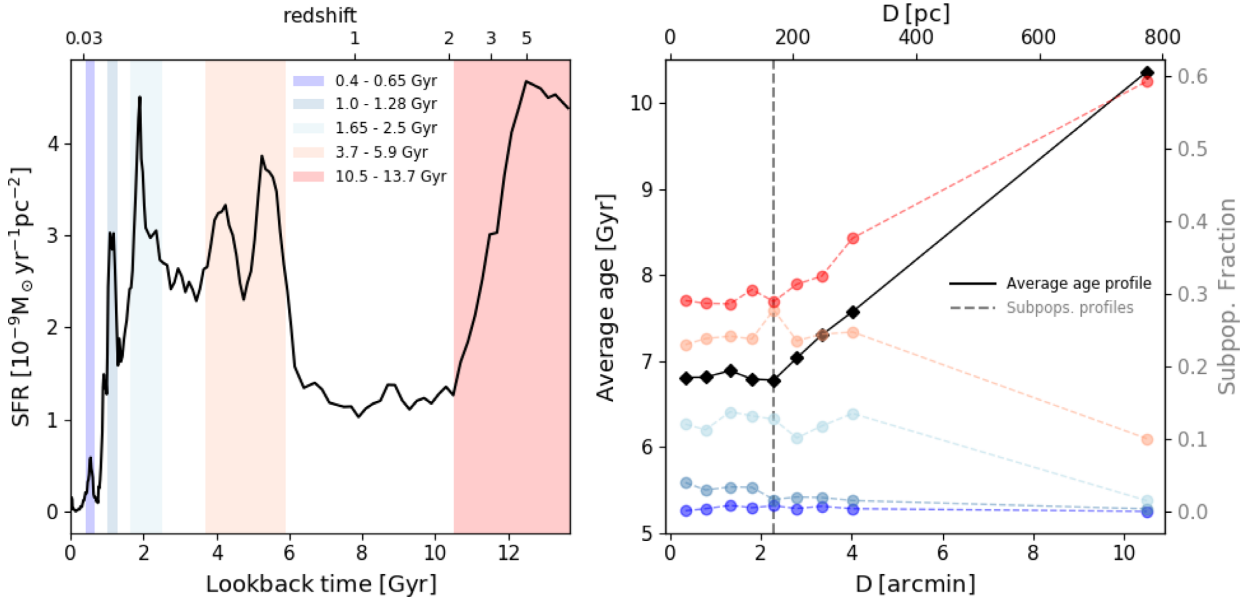


Figure 9. Stellar mean age radial profile and subpopulation spatial analysis. Left: Definition of the different stellar populations under analysis based on the SFH recovered using the whole ACS field (test A2). Right: We show the mean age profile (black, solid line; left-hand y-axis) together with fraction of stars belonging to the different stellar subpopulations defined in the left-hand panel (coloured, dashed lines; right-hand y-axis).

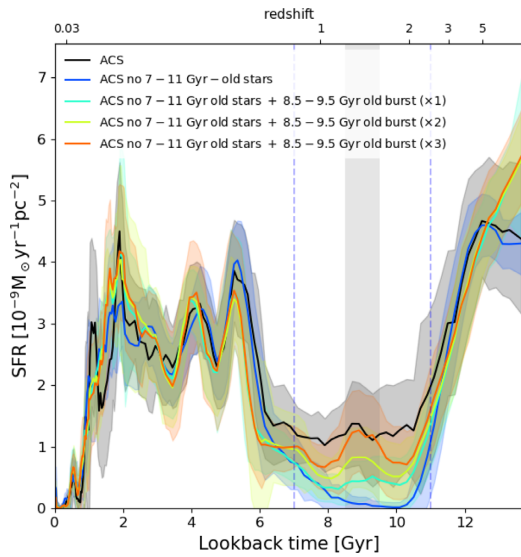


Figure 10. Characterization of the residual star formation from ~ 7 to 11 Gyr. We show the recovered SFH after analysing four mock CMDs: (i) ACS solution removing all stars with ages in the range 7–11 Gyr old (blue); (ii) same as before but including stars in the range 8.5–9.5 Gyr (cyan), as well as twice and three times that number of stars (yellow and orange, respectively). For comparison we add the ACS solution (A2, black). We highlight here that none of the tests are able to reproduce the observed behaviour (constant SFR in this age range), suggesting that a low and near-constant star formation was maintained in Leo I in this period.

Star formation was reignited again at high level in Leo I around 6 Gyr ago, nearly matching the level of SFR we measure 12 Gyr ago. There is an ample variety of processes that can result in the triggering of star formation in galactic (stellar instabilities, spiral waves, gas inflows, and global perturbations) and local scales (stellar pressure, Elmegreen 2012). In particular, galaxy mergers and interactions (both major and minor) are among the most efficient ones (Kennicutt et al.

1987; Mihos & Hernquist 1994; Hernquist & Mihos 1995; Tissera et al. 2002; Ellison et al. 2013), and it has been shown that dwarf galaxies usually undergo one major and one minor merger between redshifts 5 and 0.5, triggering star formation and disrupting their morphology (e.g. Martin et al. 2021). In this line, recent works are finding signatures of tidal interactions in the SFHs of Local Group dwarf galaxies (Miyoshi & Chiba 2020; Rusakov et al. 2020) and even in our own Galaxy (Ruiz-Lara et al. 2020).

We suggest that, based on the SFH (both the SFR as a function of time and AMR) that we recover in our analysis (see Fig. 5), star formation was reignited as a consequence of a minor merger between Leo I and another system ~ 5.5 Gyr ago. Fig. 5 shows a large dispersion on the metallicity of stars born 5–6 Gyr ago (highlighted with a brown ellipse at intermediate ages), coinciding with the peak of star formation and characterized by a clear tail towards lower metallicities (in agreement with the results from Gullieuszik et al. 2009). Both, the high SFR as well as this metal-poor tail, can be explained if a merger between Leo I and a lower mass stellar system (containing some gas) took place around that time. Such an event would have triggered star formation in Leo I from its internally processed material (responsible for the bulk of stars in that age range), and could have re-ignited star formation in the merging system as well (producing the low-metallicity tail, owing to the mass–metallicity relation and the mass difference between both systems; e.g. Erb et al. 2006; Ma et al. 2016). This would naturally explain the wide distribution of stellar metallicities found in RR Lyrae stars too (Held et al. 2001), also shown in the AMR presented in this work (see cyan ellipse in Fig. 5). In fact, Leo I is the Milky Way satellite with (by far) the broadest distribution of stellar metallicity in RR Lyrae (old) stars (Martínez-Vázquez, in preparation), and the reason for such broad distribution could be behind this merger. We hypothesize that the merging system could have been a ‘gas-containing’ ultra-faint dwarf galaxy (Willman et al. 2005) similar to the rare Leo T (Clementini et al. 2012; Weisz et al. 2012). Such a system would have hosted some of the old, low-metallicity RR Lyrae stars that we see now in Leo I, leading to the metal-poor tail reported in this work and the broad

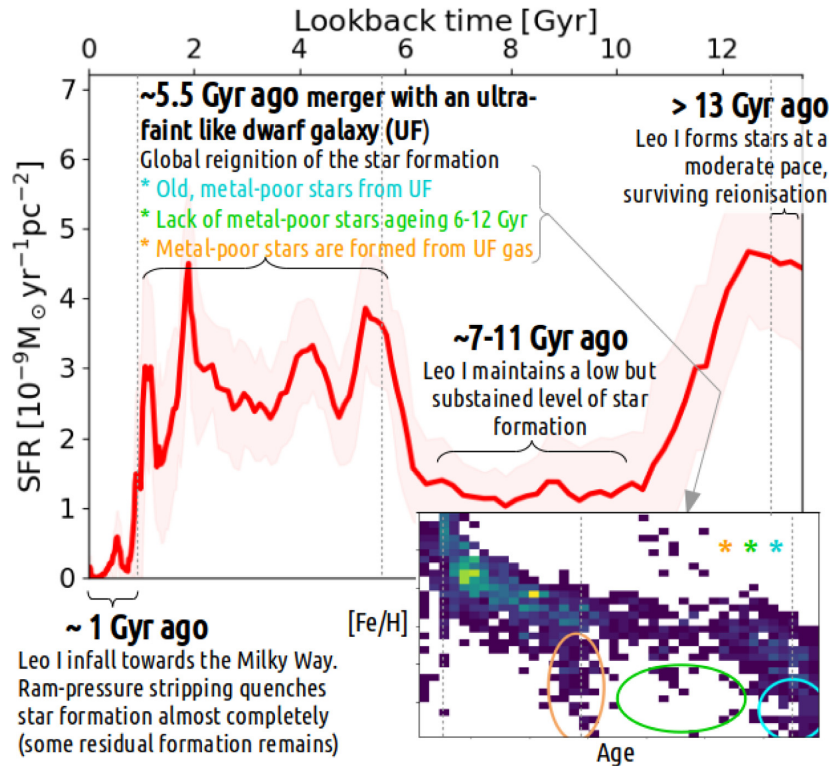


Figure 11. Scenario proposed for the temporal evolution of Leo I based on the results presented in this work.

RR Lyrae stellar metallicity distribution (Held et al. 2001; Martínez-Vázquez, in preparation). The scarcity of metal-poor stars with ages ranging from ~ 11 to 6 Gyr old suggests the dominance of old stars in this ultra-faint-like system at the time it was accreted, with its star formation being reignited at the time of the interaction. In fact, a similar behaviour is observed in the SFH of Leo T (Clementini et al. 2012, also Surot et al., in preparation), with a bursty SFR following a relatively low initial star formation activity. According to our SFH determination, at the time of the merge, Leo I possessed half of the stellar mass it has now, resulting a mass ratio between Leo I and a typical ultra-faint dwarf of 15:1, enough to re-ignite important star formation in both systems (Ruiz-Lara et al. 2020).

If this scenario was correct, one would expect that this event would have left some fingerprints not only in the chemical properties of the stars observed in Leo I, but also in kinematic (off-centred populations, comoving, and chemical families of stars, etc.) and morphological features (although to a low extent given the mass ratio of the merger). Indeed, there is no clear evidence of the presence of such structures. However, there are intriguing findings in the literature that could be related. Koch et al. (2007) found a subtle rise in the radial profile of the velocity dispersion of stars not associated with any kinematical substructure. Mateo et al. (2008) also claimed the existence of a significant velocity anisotropy for stars beyond 400 arcsec (~ 500 pc) and linked it to a previous perigalacticon passage around the Milky Way (~ 1 –2 Gyr ago). Lora et al. (2019), analysing data from Koch et al. (2007) and Bosler, Smecker-Hane & Stetson (2007), reported findings of a substructure composed by six stars ([Fe/H] from -1.78 to -1.52 dex) with low significance. In addition, we noticed some discrepancies in the exact location of the centre of this galaxy reported by different authors (Mateo et al. 2008; McConnachie 2012) as well as slight (though not significant) differences in the spatial distribution of different stellar populations

(selected in different positions of the ACS CMD). Given the low mass ratio and that signatures of such merging event might have been fully vanished by now, especially considering the close passage to the MW, we conclude that further and more detailed data are needed to properly assess this possibility. All evidence seems to support our ultra-faint-like merger scenario although we cannot discard a collision with a classical dwarf (see Fig. 11).

Finally, in agreement with previous determinations of the SFH of Leo I (Gallart et al. 1999a; Hernandez et al. 2000), star formation stopped ~ 1 Gyr ago. This time is coincident with Leo I's suggested pericentric passage to the Milky Way, as proposed from *HST* proper motion measurements (Sohn et al. 2013) and more recently using Gaia data (Fritz et al. 2018; Gaia Collaboration et al. 2018b). We conclude that, after 5 Gyr of sustained, high-level SFR, efficient ram pressure stripping from the Milky Way halo (Wetzell, Tollerud & Weisz 2015; Fillingham et al. 2016) contributed to quench star formation ~ 1 Gyr ago. Strikingly, our derived SFH suggests the presence of a small burst of star formation around 0.5 Gyr ago. Indeed, the careful analysis of the CMD of Leo I (carried out in Section 3) shows the presence of stars as young as 100 Myr. These findings are in line to the recent work by Hausammann, Revaz & Jablonka (2019). The authors, using hydrodynamical simulations, show that while ram-pressure efficiently strips hot and diffuse gas from the incoming dwarf systems, the cold gas may remain and be compressed, enhancing (a small tail) of star formation. Cold gas stripping will depend on the ratio between the thermal pressure and the ram pressure applied to the dwarf by the hot halo gas: if the thermal pressure is high, cold gas can be retained and even compressed to form new stars. In other words, the presence of stars younger than 1 Gyr (pericentric passage) in Leo I suggests that the thermal pressure during the approach was high, implying a hot and dense Milky Way halo.

The radial analysis presented in Section 5 adds another dimension to this study. On one hand, it shows that one must be cautious when extracting global conclusions based on a CMD not covering most of the analysed system, as spatial variations might bias the conclusions. Bermejo-Climent et al. (2018) computed the total mass formed in stars by $z = 2$ for a sample of 16 Local Group dwarf galaxies taking into account the fraction of old stars that was being missed in SFH studies due to their limited spatial coverage and presence of age gradients. In the same line, Graus et al. (2019) suggested that the SFH recovered from a region around the half-light radius of a system would be representative of its global SFH. The similarities between what we call global SFH determined in Section 4 (see Fig. 4) and that of region 7 in Section 5 (see Fig. 8), located near the half-light radius both support the findings by Graus et al. (2019) and confirm the validity of the discussion so far. On the other hand, adding the spatial dimension to SFH studies poses important constraints to theoretical simulations on galaxy formation and evolution, allowing a better understanding on the physics governing dwarf galaxy evolution.

Fig. 8 and specially Fig. 9 show a clear dominance of progressively older populations as we move outwards in Leo I (in agreement with Held et al. 2000; Gullieuszik et al. 2009). Strikingly, the inner ~ 190 pc of Leo I seems to be fairly uniform, displaying very similar SFHs and the same census of stellar populations (see right-hand panel of Fig. 9). Stinson et al. (2009), making use of smooth particle hydrodynamic simulations, found that elevated early star formation activity combined with supernova feedback could lead to: (i) the shrinking of the gaseous star forming disc; and, (ii) the ejection of stars to the outer parts. This would inevitably cause the appearance of positive age gradients and the accumulation of old stars in the outskirts of dwarf galaxies. The combination of both effects might well be the main reason behind the positive age gradient displayed by the outer regions of Leo I, with different importance at different radius. Given the relative homogeneity of the SFHs in the inner parts of Leo I, and the contrast between inner and outer parts in the last 5 Gyr, we could conclude that the gaseous star forming disc after the time of the last merger (~ 4.5 Gyr ago) had a radius of ~ 190 pc.

However, we find clear evidence suggesting that at least regions 5–8 were not totally depleted of gas after that early time, since conspicuous peaks of star formation are found in them at ~ 13 , 5.5, 2.0, and 1.0 Gyr ago. In these regions, the amount of star formation that occurred at these epochs is substantial, and clearly implies the presence of gas. However, its natural state and the physical conditions of the gas may have not allowed sustained star formation, and only when external effects came into play, star formation was triggered. That was the case 5.5 Gyr ago (proposed merger with an ultra-faint-like dwarf system) and 1 Gyr ago (perigalacticon passage). The peak at 2 Gyr still remains a mystery. Nevertheless, the intensity of the 2-Gyr star forming peak, and its presence in the whole region under analysis (up to ~ 750 pc) propose another possible event to be unveiled in the past history of Leo I. The situation may be different in region 9, which may be representative of the far outskirts of Leo I near its tidal radius. In this region, while enhancements in the SFR at ~ 5.5 , 2.0, and 1.0 Gyr ago are still noticeable, they are less prominent, and possibly linked to the ejection of stars to the outer parts via stellar feedback rather than merger-induced star formation (Graus et al. 2019).

7 CONCLUSIONS

In this work, we have thoroughly analysed the deepest available *HST* CMDs of the Leo I dwarf galaxy. These CMDs reach the oldest main-sequence turn-offs with photometry of excellent quality, and

cover a wide spatial extension of this galaxy. The combination of this data set, together with state-of-the-art CMD fitting techniques and stellar evolutionary models, has allowed us to obtain a unprecedented detailed view of the past history of this interesting dwarf galaxy (see Fig. 11). Our findings can be summarized as follows:

(i) Leo I has been able to maintain an extended and episodic star formation until ~ 1 Gyr ago, when star formation quenched, possibly as a consequence of ram pressure stripping induced by the halo of the Milky Way after the latest pericentric passage. The absence of gas in Leo I (Knapp et al. 1978; Grcevich & Putman 2009), together with its SFH may indicate that this dwarf galaxy has just finished its transition from dIrr to dSph.

(ii) Conspicuous and recurrent peaks of star formation are found throughout Leo I at ~ 13 , 5.5, 2.0, and 1.0 Gyr ago. The spatial extension of such bursts suggests a violent and external origin for recent ones, while the oldest one should correspond to the early phases of star formation in the system.

(iii) We find evidence of a wet merger ~ 5.5 Gyr ago with an ultra-faint dwarf-like stellar system, responsible for such a star forming burst and the presence of extremely metal-poor stars in Leo I.

(iv) We hypothesize that another important event should have taken place ~ 2 Gyr ago, giving rise to one of the most efficient star forming events in Leo I.

(v) Residual star formation in the last Gyr (after Leo I's pericentric passage) suggest that cold gas survived ram pressure stripping, implying that the Milky Way halo was hot and dense at the moment of the encounter.

(vi) We find two clearly differentiated regions within Leo I. The inner ~ 190 pc present a quite homogeneous distribution of its stellar populations, displaying a very similar SFH. This may be the size of the star forming gaseous disc after the last large merger (~ 4.5 Gyr ago). The outer parts are characterized by a positive age gradient, with old populations dominating the outer parts, possibly as a consequence of the shrinking of the star forming gaseous disc and radial ejection of stars.

Further studies as the one presented in this work, linking global with spatially resolved SFHs, are of the utmost importance. They do not only permit an unprecedented characterization of past events in the history of individual galaxies, they also allow to set further constraints on low-mass galaxy simulations and the modelling of baryonic physics. This will significantly improve our knowledge on how dwarf galaxies form and evolve.

ACKNOWLEDGEMENTS

We thank the anonymous referee for useful comments improving the original version of this manuscript. TRL, MM, CG, TKF, and GB acknowledge financial support through the grant AYA2017-89076-P (AEI/FEDER, UE) as well as by the Ministerio de Ciencia, Innovación y Universidades (MCIU), through the State Budget and by the Consejería de Economía, Industria, Comercio y Conocimiento of the Canary Islands Autonomous Community, through the Regional Budget (including IAC projects, ‘The Local Group in multi-dimensions’ and TRACES). TRL acknowledges support from a Spinoza grant (NWO) awarded to A. Helmi. TRL is also supported by grant AYA2016-77237-C3-1-P (RAVET project), an MCIU Juan de la Cierva – Formación grant (FJCI-2016-30342) and acknowledges support from the Spanish Public State Employment Service (SEPE). This research has been partially supported by the Spanish projects PID2019-104928RB-I00 (MINECO/FEDER, UE) and ProID2017010132 (Gobierno de

Canarias/FEDER, UE). SC acknowledges support from Premiale INAF ‘MITIC’ and grant AYA2013-42781P from the Ministry of Economy and Competitiveness of Spain, he has also been supported by INFN (Iniziativa specifica TASP). This research makes use of PYTHON (<http://www.python.org>); MATPLOTLIB (Hunter 2007), a suite of open-source PYTHON modules that provide a framework for creating scientific plots; and ASTROPY, a community-developed core PYTHON package for Astronomy (Astropy Collaboration 2013, 2018).

DATA AVAILABILITY

The main data set analysed in this article is publicly available and can be retrieved from the *HST* archive webpage (<https://archive.stsci.edu/hst/>) under programmes GO10520 and GO12270. Fully reduced photometry, artificial star tests, synthetic CMDs, and star formation histories consequence of this analysis will be shared on reasonable request to the corresponding author.

REFERENCES

- Astropy Collaboration, 2013, *A&A*, 558, A33
 Astropy Collaboration, 2018, *AJ*, 156, 123
 Battaglia G. et al., 2006, *A&A*, 459, 423
 Battaglia G., Rejkuba M., Tolstoy E., Irwin M. J., Beccari G., 2012a, *MNRAS*, 424, 1113
 Battaglia G., Irwin M., Tolstoy E., de Boer T., Mateo M., 2012b, *ApJ*, 761, L31
 Beccari G. et al., 2014, *A&A*, 570, A78
 Bellazzini M., Gennari N., Ferraro F. R., Sollima A., 2004, *MNRAS*, 354, 708
 Belloni D., Askar A., Giersz M., Kroupa P., Rocha-Pinto H. J., 2017, *MNRAS*, 471, 2812
 Belokurov V. et al., 2007, *ApJ*, 654, 897
 Benítez-Llambay A., Navarro J. F., Abadi M. G., Gottlöber S., Yepes G., Hoffman Y., Steinmetz M., 2015, *MNRAS*, 450, 4207
 Bermejo-Clement J. R. et al., 2018, *MNRAS*, 479, 1514
 Bernard E. J. et al., 2008, *ApJ*, 678, L21
 Bernard E. J., Ferguson A. M. N., Chapman S. C., Ibata R. A., Irwin M. J., Lewis G. F., McConnachie A. W., 2015, *MNRAS*, 453, L113
 Bernard E. J., Schultheis M., Di Matteo P., Hill V., Haywood M., Calamida A., 2018, *MNRAS*, 477, 3507
 Bosler T. L., Smecker-Hane T. A., Stetson P. B., 2007, *MNRAS*, 378, 318
 Boylan-Kolchin M., Bullock J. S., Kaplinghat M., 2011, *MNRAS*, 415, L40
 Cash W., 1979, *ApJ*, 228, 939
 Cassisi S., Potekhin A. Y., Pietrinfermi A., Catelan M., Salaris M., 2007, *ApJ*, 661, 1094
 Clementini G., Cignoni M., Contreras Ramos R., Federici L., Ripepi V., Marconi M., Tosi M., Musella I., 2012, *ApJ*, 756, 108
 Cole A. A. et al., 2007, *ApJ*, 659, L17
 Cole A. A., Weisz D. R., Dolphin A. E., Skillman E. D., McConnachie A. W., Brooks A. M., Leaman R., 2014, *ApJ*, 795, 54
 Dayal P., Ferrara A., 2018, *Phys. Rep.*, 780, 1
 del Pino A., Aparicio A., Hidalgo S. L., 2015, *MNRAS*, 454, 3996
 Di Cintio A., Brook C. B., Macciò A. V., Stinson G. S., Knebe A., Dutton A. A., Wadsley J., 2014, *MNRAS*, 437, 415
 Dolphin A. E., 2002, *MNRAS*, 332, 91
 Dutton A. A. et al., 2016, *MNRAS*, 461, 2658
 Efstathiou G., 1992, *MNRAS*, 256, 43P
 Ellison S. L., Mendel J. T., Patton D. R., Scudder J. M., 2013, *MNRAS*, 435, 3627
 Elmegreen B. G., 2012, in Tuffs R. J., Popescu C. C., eds, Proc. IAU Symp. 284, The Spectral Energy Distribution of Galaxies – SED 2011. p. 317
 Erb D. K., Shapley A. E., Pettini M., Steidel C. C., Reddy N. A., Adelberger K. L., 2006, *ApJ*, 644, 813
 Faria D., Feltzing S., Lundström I., Gilmore G., Wahlgren G. M., Ardeberg A., Linde P., 2007, *A&A*, 465, 357
 Fillingham S. P., Cooper M. C., Pace A. B., Boylan-Kolchin M., Bullock J. S., Garrison-Kimmel S., Wheeler C., 2016, *MNRAS*, 463, 1916
 Fritz T. K., Battaglia G., Pawlowski M. S., Kallivayalil N., van der Marel R., Sohn S. T., Brook C., Besla G., 2018, *A&A*, 619, A103
 Gaia Collaboration, 2018a, *A&A*, 616, A1
 Gaia Collaboration, 2018b, *A&A*, 616, A12
 Gallart C., Freedman W. L., Aparicio A., Bertelli G., Chiosi C., 1999a, *AJ*, 118, 2245
 Gallart C. et al., 1999b, *ApJ*, 514, 665
 Gallart C. et al., 2015, *ApJ*, 811, L18
 Gnedin N. Y., 2000, *ApJ*, 542, 535
 Graus A. S. et al., 2019, *MNRAS*, 490, 1186
 Grcevich J., Putman M. E., 2009, *ApJ*, 696, 385
 Grebel E. K., 1999, in Whitelock P., Cannon R., eds, Proc. IAU Symp. 192, The Stellar Content of Local Group Galaxies. Astronomical Society of the Pacific, San Francisco, CA, p. 17
 Gullieuszik M., Held E. V., Saviane I., Rizzi L., 2009, *A&A*, 500, 735
 Harbeck D. et al., 2001, *AJ*, 122, 3092
 Hausammann L., Revaz Y., Jablonka P., 2019, *A&A*, 624, A11
 Held E. V., Saviane I., Momany Y., Carraro G., 2000, *ApJ*, 530, L85
 Held E. V., Clementini G., Rizzi L., Momany Y., Saviane I., Di Fabrizio L., 2001, *ApJ*, 562, L39
 Held E. V., Gullieuszik M., Rizzi L., Girardi L., Marigo P., Saviane I., 2010, *MNRAS*, 404, 1475
 Hernandez X., Gilmore G., Valls-Gabaud D., 2000, *MNRAS*, 317, 831
 Hernquist L., Mihos J. C., 1995, *ApJ*, 448, 41
 Hidalgo S. L. et al., 2011, *ApJ*, 730, 14
 Hidalgo S. L. et al., 2013, *ApJ*, 778, 103
 Hidalgo S. L. et al., 2018, *ApJ*, 856, 125
 Hoefl M., Yepes G., Gottlöber S., Springel V., 2006, *MNRAS*, 371, 401
 Hunter J. D., 2007, *Comput. Sci. Eng.*, 9, 90
 Irwin M., Hatzidimitriou D., 1995, *MNRAS*, 277, 1354
 Kennicutt R. C., Jr, Keel W. C., van der Hulst J. M., Hummel E., Roettiger K. A., 1987, *AJ*, 93, 1011
 Kirby E. N. et al., 2010, *ApJS*, 191, 352
 Kirby E. N., Lanfranchi G. A., Simon J. D., Cohen J. G., Guhathakurta P., 2011, *ApJ*, 727, 78
 Kirby E. N., Cohen J. G., Guhathakurta P., Cheng L., Bullock J. S., Gallazzi A., 2013, *ApJ*, 779, 102
 Knapp G. R., Kerr F. J., Bowers P. F., 1978, *AJ*, 83, 360
 Koch A., Wilkinson M. I., Kleyna J. T., Gilmore G. F., Grebel E. K., Mackey A. D., Evans N. W., Wyse R. F. G., 2007, *ApJ*, 657, 241
 Kroupa P., 2001, *MNRAS*, 322, 231
 Lee M. G., Freedman W., Mateo M., Thompson I., Roth M., Ruiz M.-T., 1993, *AJ*, 106, 1420
 Lora V., Grebel E. K., Schmeja S., Koch A., 2019, *ApJ*, 878, 152
 Ma X., Hopkins P. F., Faucher-Giguère C.-A., Zolman N., Muratov A. L., Kereš D., Quataert E., 2016, *MNRAS*, 456, 2140
 Martin G. et al., 2021, *MNRAS*, 500, 4937
 Martínez-Vázquez C. E. et al., 2015, *MNRAS*, 454, 1509
 Mateo M. L., 1998, *ARA&A*, 36, 435
 Mateo M., Olszewski E. W., Walker M. G., 2008, *ApJ*, 675, 201
 McConnachie A. W., 2012, *AJ*, 144, 4
 McMonigal B. et al., 2014, *MNRAS*, 444, 3139
 Mihos J. C., Hernquist L., 1994, *ApJ*, 425, L13
 Miyoshi T., Chiba M., 2020, preprint ([arXiv:2003.07006](https://arxiv.org/abs/2003.07006))
 Monelli M. et al., 2010a, *ApJ*, 720, 1225
 Monelli M. et al., 2010b, *ApJ*, 722, 1864
 Monelli M. et al., 2016, *ApJ*, 819, 147
 Muñoz R. R., Côté P., Santana F. A., Geha M., Simon J. D., Oyarzún G. A., Stetson P. B., Djorgovski S. G., 2018, *ApJ*, 860, 66
 Okamoto T., Gao L., Theuns T., 2008, *MNRAS*, 390, 920
 Okamoto S., Arimoto N., Tolstoy E., Jablonka P., Irwin M. J., Komiyama Y., Yamada Y., Onodera M., 2017, *MNRAS*, 467, 208
 Peebles P. J. E., 1965, *ApJ*, 142, 1317

- Pietrinferni A., Cassisi S., Salaris M., Castelli F., 2004, *ApJ*, 612, 168
- Planck Collaboration XLVII, 2016, *A&A*, 596, A108
- Ruiz-Lara T. et al., 2018, *A&A*, 617, A18
- Ruiz-Lara T., Gallart C., Bernard E. J., Cassisi S., 2020, *Nat. Astron.*, 4, 965
- Rusakov V., Monelli M., Gallart C., Fritz T. K., Ruiz-Lara T., Bernard E. J., Cassisi S., 2020, preprint (arXiv:2002.09714)
- Santana F. A. et al., 2016, *ApJ*, 829, 86
- Savino A., Tolstoy E., Salaris M., Monelli M., de Boer T. J. L., 2019, *A&A*, 630, A116
- Silk J., Mamon G. A., 2012, *Res. Astron. Astrophys.*, 12, 917
- Sohn S. T., Besla G., van der Marel R. P., Boylan-Kolchin M., Majewski S. R., Bullock J. S., 2013, *ApJ*, 768, 139
- Stetson P. B., 1987, *PASP*, 99, 191
- Stetson P. B., 1994, *PASP*, 106, 250
- Stinson G. S., Dalcanton J. J., Quinn T., Gogarten S. M., Kaufmann T., Wadsley J., 2009, *MNRAS*, 395, 1455
- Tissera P. B., Domínguez-Tenreiro R., Scannapieco C., Sáiz A., 2002, *MNRAS*, 333, 327
- Tolstoy E. et al., 2004, *ApJ*, 617, L119
- Tolstoy E., Hill V., Tosi M., 2009, *ARA&A*, 47, 371
- Weisz D. R. et al., 2011, *ApJ*, 739, 5
- Weisz D. R. et al., 2012, *ApJ*, 748, 88
- Weisz D. R., Dolphin A. E., Skillman E. D., Holtzman J., Gilbert K. M., Dalcanton J. J., Williams B. F., 2014a, *ApJ*, 789, 147
- Weisz D. R., Dolphin A. E., Skillman E. D., Holtzman J., Gilbert K. M., Dalcanton J. J., Williams B. F., 2014b, *ApJ*, 789, 148
- Weisz D. R., Dolphin A. E., Skillman E. D., Holtzman J., Gilbert K. M., Dalcanton J. J., Williams B. F., 2015, *ApJ*, 804, 136
- Wetzel A. R., Tollerud E. J., Weisz D. R., 2015, *ApJ*, 808, L27
- Willman B. et al., 2005, *AJ*, 129, 2692

APPENDIX A: ON THE RELIABILITY OF THE RECOVERED SFHS: TESTING THE ROBUSTNESS OF THE METHOD

The fine details of the recovered SFH of a stellar system via CMD fitting might be, in principle, influenced by the details of the used synthetic CMD as well as the adopted bundle strategy for the comparison. In this appendix, we assess the effects of these choices on our results, and evaluate the robustness and reliability of our SFH determination by comparing a number of realizations exploring different input parameters. Due to the large number of stars within the ACS field, we decided to carry out these tests using the CMD from this field (containing 191 756 stars).

All the tests and their main peculiarities are described in Table A1 and Fig. A1. In short, six different synthetic diagrams (all using the BaSTI isochrones; Pietrinferni et al. 2004) are computed assuming different unresolved binary fractions (β) and minimum mass ratios for binaries (q , denoted by number from 1 to 6). In addition, four different bundle strategies have been used for each of the six synthetic CMDs, covering most of the stars with $M_{F814W} < 4.5$ (denoted by letters from A to D). In total, 24 different tests are compared to single out the optimal strategy.

Binary stars are common in the Galactic field as well as in local dwarf galaxies. Thus, the way we incorporate them in the synthetic CMDs might affect the final SFH recovery (Gallart et al. 1999a; Belloni et al. 2017). For this reason, we test different unresolved binary fractions (β of 0.3, 0.5, and 0.7) and different minimum mass ratios (q of 0.1, allowing for stars of very different masses in the pairs; and q of 0.4, restricting to stars of similar mass in the pair). Fig. A2 shows the χ^2 of the 24 different tests distinguishing between different binary populations (line styles and x -axis) and

bundle strategy (colours). In general, lower values of χ^2 are found in the case of $q = 0.1$ and β of 0.3–0.5 (with 0.5 being slightly preferred). Careful examination of the fit residuals in the colour–magnitude plane shows the presence of a clear, doubled MS when $q = 0.4$ is used, suggesting that Leo I hosts binaries with members of very different masses and arguing against this particular value. These tests clearly show that configuration number 2, $q = 0.1$ and $\beta = 0.5$, is preferred.

In the adopted methodology, the bundle strategy determines the regions of the diagram from which information is extracted to recover the SFH. In general, one might think that avoiding regions of the CMD containing stars in less-understood and advanced stellar evolutionary phases or regions suffering from higher age–metallicity degeneracy should be favoured. Tests A–D expands on this. Strategy A represents an approach in which most of the CMD is considered for the fit, with the MS having more importance than other regions. In the cases B and D, we include the sub-giant within the MS bundle and fit or avoid the RC area. Strategy C adopts a single bundle well sampled with the use of small boxes.

A direct comparison of the different χ^2 values recovered to determine the best bundle strategy (as done before) would not be appropriate. THESTORM ultimately relies on the minimization of the χ^2 function described in Cash (1979):

$$\chi^2 = 2 \sum_j (M^j - O^j \ln M^j), \quad (\text{A1})$$

where M and O would correspond to the model and observed CMDs, respectively, and j would run over all the boxes defined. As such, all the colour–magnitude boxes in which we divide the CMDs for the fit will contribute to the final χ^2 , affecting its value (see tables in Fig. A1, and Section 4). As a consequence, given the different number of boxes among strategies and CMD coverage (see Fig. A1), we cannot simply compare χ^2 values to assess the suitability of one strategy over the other. For this reason, and following a criterion previously used in Ruiz-Lara et al. (2018), the choice of the bundle strategy is made based on the comparison between the metallicity distributions (RGB region) that we find in each attempt with that observed for RGB stars by Kirby et al. 2011 (see also Kirby et al. 2010), based on spectral synthesis of iron absorption lines. Fig. A3 compares the [Fe/H] distribution of RGB stars within the ACS field of view determined by Kirby et al. (2011) and the distributions inferred using the different strategies (using always synthetic CMD #2). We should clarify at this point that, for the comparison, we have used only RGB stars in the same range of magnitudes as that covered by Kirby et al. (2011). Although all distributions are fairly compatible (especially considering the difficulty of reproducing the exact metallicity distribution of RGB stars from CMD fitting), configuration A is the one that results in a RGB metallicity distribution that better resembles the one found by Kirby et al. (2011).

Adding the bundle strategy information to the one regarding the binary population we conclude that, among all the tests, A2 is preferred over the rest. Thus, all the analysis presented in the main body of the paper is based on this choice. As can be seen in Fig. 4 (black lines), all different tests are compatible within errors and the same different star formation bursts defined in Section 4 are found in all tests, highlighting the robustness and stability of this implementation of the CMD fitting technique. The analysis presented in this appendix allows us to claim that the results presented in this work are not contingent on the particular set of input parameters used in the recovery of SFHs.

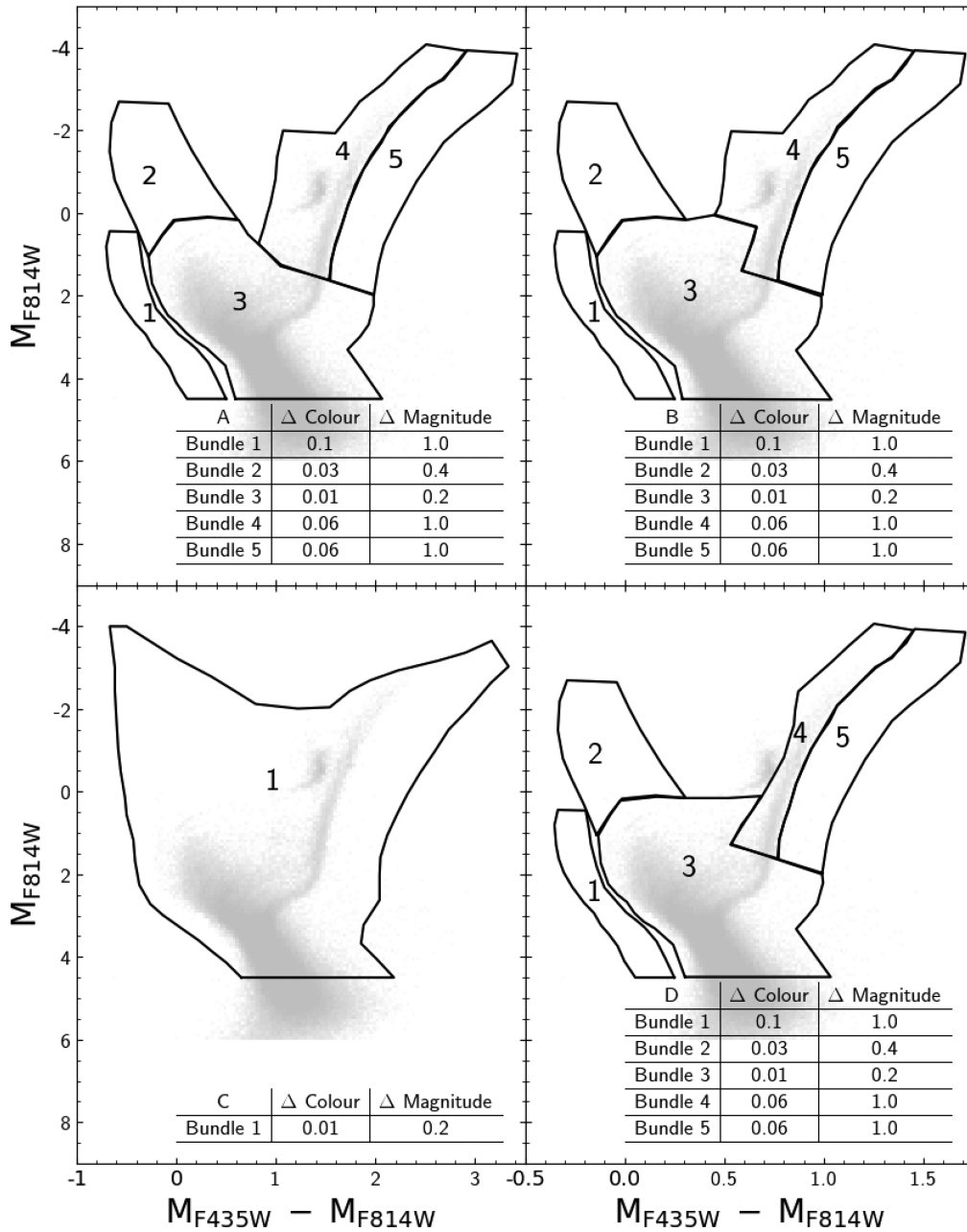


Figure A1. SFH recovery tests, bundle strategy. This figure depicts the different bundle strategies examined during this work. The inset tables indicate the dimensions of the boxes in which the different bundles are divided for the star counting (see Section 4).

Table A1. SFH recovery tests. The 24 different realizations analysed during these tests are the combinations of (i) six different unresolved binary fraction (β) and minimum mass ratio for binaries (q) as well as (ii) four different bundle strategies regarding the inclusion and sampling of the RC, RGB, and sub-giant region (see also Fig. A1).

Synthetic CMD test	q	β	Bundle strategy	Bundle description
1	0.1	0.3	A	MS in small boxes, sub-giant + RGB + RC in big boxes
2	0.1	0.5	B	Similar to A + sub-giant in small boxes
3	0.1	0.7	C	Whole CMD in small boxes
4	0.4	0.3	D	Similar to B, but avoiding the RC
5	0.4	0.5		
6	0.4	0.7		

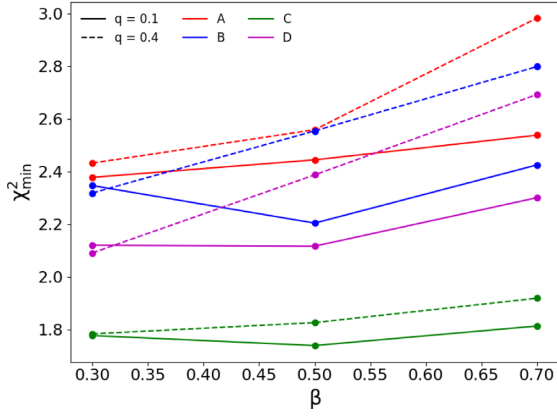


Figure A2. Variation of χ^2 as a function of the unresolved binary fraction (β) for different minimum binary mass ratios (solid lines for $q = 0.1$ and dashed lines for $q = 0.4$) and different bundle strategies (red for A, blue for B, green for C, and magenta for D).

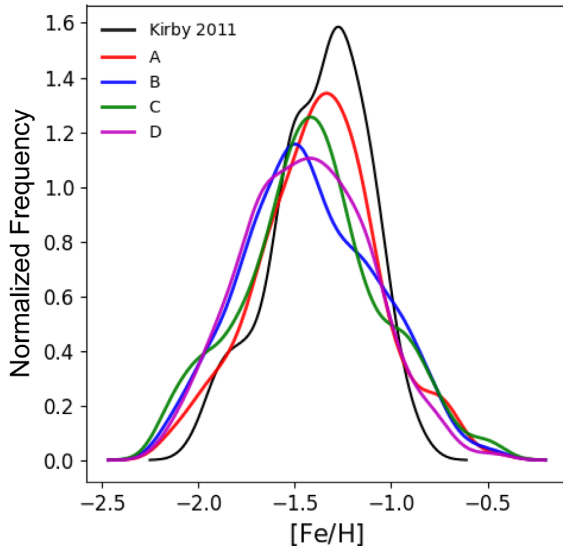


Figure A3. [Fe/H] distribution of RGB stars within the ACS field of view from Kirby et al. (2011, black line) and from different bundle strategies using synthetic CMD number 2 (red for A, blue for B, green for C, and magenta for D).

APPENDIX B: DisPar: SIMULATING OBSERVATIONAL EFFECTS ON SYNTHETIC COLOUR-MAGNITUDE DIAGRAMS

Before comparing the observed CMDs (from which we want to derive the SFH) with the set of SSPs extracted from the synthetic CMD (as described in Section 4), it is necessary to use the information on incompleteness and photometric errors affecting the observed CMDs (and derived from the ASTs, see Section 2.1, as a function of both position in the CMD and physical position in the sky) to simulate uncertainties in the error-free synthetic CMDs. This error simulation is a key step towards the determination of SFHs as observational effects are able to affect the actual colours and magnitudes of observed stars, measuring colour and magnitude values far from the real ones (especially important at faint magnitudes below the oldest MSTO, see Fig. B1 and Gallart et al. 1999a). The simulation

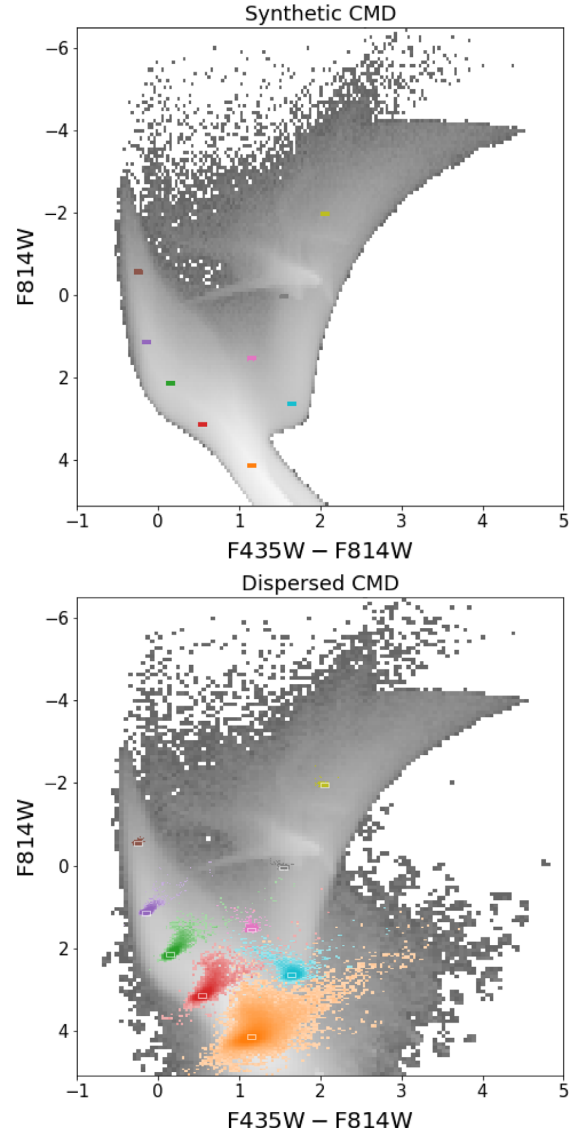


Figure B1. Error simulation with DisPar. Left-hand panel: synthetic CMD number 2 before error simulation, some particular regions are highlighted in different colours. Right-hand panel: same synthetic CMD after simulating photometric errors taking into account artificial star tests (see Section 2.1) using DisPar. The coloured density maps represent the position of the synthetic stars highlighted in the left-hand panel after the error simulation. As expected, fainter stars are more affected by crowding and photometric errors than brighter stars.

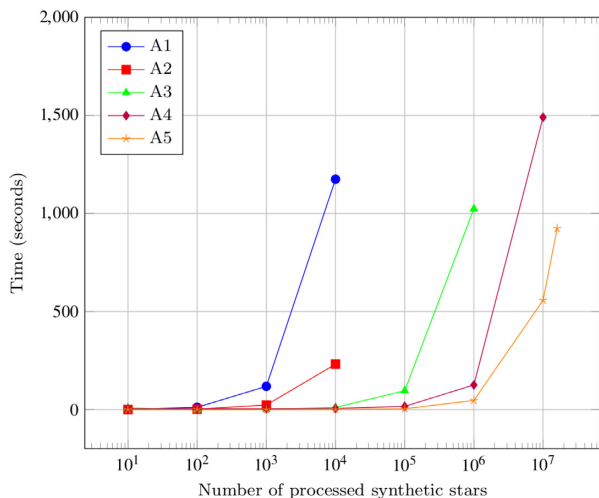
of observational effects is done using a specifically designed code named DisPar. In what follows, we provide a short description on the practical procedure as well as the technical details behind DisPar.

DisPar goes through each and every star in the synthetic CMD of magnitudes ($M1_s, M2_s$) and position (X_s, Y_s).⁸ For each synthetic

⁸For explanatory purposes, we will generalize to magnitudes $M1$ and $M2$ (generic filters 1 and 2) and positions X and Y . The spatial distribution of observed stars in the sky (X, Y) is simulated in the synthetic CMD as well. In the particular case of this paper, we use filters $F435W$ and $F814W$ (ACS); and $F438W$ and $F814W$ (WFC3). For the positions in the sky we use pixels (image coordinates). Sky coordinates (RA, Dec.) could be used as well.

Table B1. Computing times for the different dispersion algorithms.

nStars	A1	A2	A3	A4	A5
10	1.1139	0.2796	8.5115	4.5686	0.1332
100	11.6606	2.5325	0.1615	4.7227	0.2156
1000	118.5543	23.4513	1.3283	4.7142	0.33
10000	1175.1146	231.5997	11.1537	5.8857	0.464
100 000	–	–	96.0288	16.4766	4.4536
1000 000	–	–	1024.29	125.6757	46.5718
10 000 000	–	–	–	1490.7665	557.6948
16 000 000	–	–	–	–	923.8403


Figure B2. Evolution of the computing times for the different dispersion algorithms.

star, it considers all artificial stars from the ASTs within user-defined colour–magnitude ($[col, mag] = [0.06, 0.1]$ in this particular case) and position boxes ($[X, Y] = [200px, 200px]$) with input and recovered magnitudes ($M1_i, M2_i$) and ($M1_r, M2_r$), respectively, and input position (X_i, Y_i). If a minimum number of artificial stars is found within the boxes (user-defined, 10 in this case), one is randomly selected and the magnitudes of the synthetic stars under consideration are modified accordingly, $M1'_s = M1_s - (M1_i - M1_r)$ and $M2'_s = M2_s - (M2_i - M2_r)$. In the case that this minimum number of artificial stars requirement is not fulfilled, the size of the boxes is doubled and the search starts again. If the synthetic star has no counterpart in the ASTs, its magnitudes are not modified and the star is flagged in the output file containing the dispersed CMD. An example of `DisPar` applied to synthetic CMD number 2 is shown in Fig. B1.

`DisPar` algorithm basically performs searches in an efficient way. To this end, it relies on two key factors:

- (i) the use of a data structure that allows to perform quick searches,
- (ii) and the parallelization of the code.

Note that, if the number of synthetic stars is m and the number of artificial stars is n , the complexity of a straight forward search is $O(mn)$ ⁹ since, in the worst case, for any of the m synthetic stars, all

the n artificial stars must be checked to look for the defined number of similar ones. This complexity can be reduced by using some data structure that eases the searches, such as AVL trees. An AVL tree is a binary search tree in which the difference between the heights of the left and right subtrees of any node is less than or equal to one. On such structure, the insertion, deletion, rebalancing, and searching operations can all be performed in $O(\log n)$, being n the data size.

When comparing the synthetic and artificial stars, four criteria are taken into account (position in the CMD, position in the sky). To this end, we created a custom data structure consisting of four nested AVL trees, one for each searching criteria. Moreover, for the sake of computational efficiency, the resulting dynamic data structure is then ‘flattened’, that is, each nested AVL tree is stored in an array, preserving relations between trees. As a result of these improvements, the computational complexity of `DisPar` is set to $O(m \log n)$.

Finally, `DisPar` was coded in C/C++ in three different ways, using parallel programming. The source code of the different implementations, as well as the description of the input files and parameters, and a user manual (so far only in Spanish, currently working on the English version), are available at the public repository <https://bitbucket.org/ULLfypIAC/workspace/projects/FYP>.

The `DisPar` version used in this paper runs on multicore CPUs using OpenMP. Another version allows to choose between running on Nvidia GPUs using the CUDA programming model, or on multicore CPUs using OpenMP. Both versions can be found in folder `crowding-effects-cli-iterative` and receive as input plain text files. The third version of the code uses also OpenMP and allows to modify the set of searching criteria, at the cost of losing some computational speed. This code receives as input a JSON file, and it is placed in folder `crowding-effects-cli-recursive`.

To evaluate the performance of `DisPar`, we conducted several computational experiments on a data set with nearly 12 000 000 artificial stars and a number of synthetic stars ranging from 10 to 16 000 000. All the experiments were carried out on a PC under Kubuntu with a processor Intel Core i7-4930K at 3.4 GHz, 32 GB of RAM, and graphic card Nvidia GeForce Titan Black, GPU GK110, at 967 MHz, with 2880 CUDA cores and a 6 GB VRAM. A time limit of 2000 s was imposed to each run. The results are displayed in Table B1. Column *nStars* shows the number of synthetic stars used in each experiment. The remaining columns show computing times in seconds for the following dispersion algorithms:

⁹The so-called big O notation is used in computer science to classify algorithms according to how their run time requirements (or *time complexity*) grow as the input size grows. An algorithm is said to be $O(f(n))$ if its time complexity doesn’t grow faster than function $f(n)$, being n the input size.

- (i) *A1*: Sequential $O(mn)$ basic algorithm.
- (ii) *A2*: $O(mn)$ basic algorithm parallelized using OpenMP.
- (iii) *A3*: `DisPar` OpenMP algorithm with possibility of choosing the set of searching criteria.
- (iv) *A4*: `DisPar` OpenMP algorithm with fixed number of searching criteria (4).
- (v) *A5*: `DisPar` CUDA algorithm with fixed number of searching criteria (4).

A blank space in the table means that the algorithm has failed to fulfil the dispersion problem within the time limit. Fig. B2 shows the

evolution of the computing times of the different algorithms as the number of synthetic stars increases. These results show that `DisPar` clearly outperforms the basic dispersion algorithm, and that it is able to cope with the dispersion problem for a large number of stars at a reasonable computational effort.

This paper has been typeset from a $\text{\TeX}/\text{\LaTeX}$ file prepared by the author.